JSR

Journal of Sedimentary Research, 2025, v. 95, 707–722
Research Article
DOI: 10.2110/jsr.2024.155

REDOX DYNAMICS AND METAL CYCLING IN THE CARBONATE-BUFFERED SEDIMENT–WATER INTERFACE OF THE FERRUGINOUS AND SULFATIC LAKE MEDARD, CZECH REPUBLIC

DANIEL A. PETRASH,[1,2] ASTOLFO VALERO,[2] KARELYS UMBRÍA-SALINAS,[2] CHRISTOPHE THOMAZO,[3,4] TRAVIS B. MEADOR,[2,5] FRANTIŠEK LAUFEK,[1] JAMES J. VALDÉS,[2] VLADISLAV CHRASTNÝ,[6] AND KURT O. KONHAUSER[7]

[1]*Czech Geological Survey, 152 00 Prague, Czech Republic*
[2]*Biology Centre, Czech Academy of Sciences, 370 05 České Budějovice, Czech Republic*
[3]*UMR CNRS 6282 Biogeosciences, University of Burgundy, 21000 Dijon, France*
[4]*Institut Universitaire de France, 75000 Paris, France*
[5]*Faculty of Science, University of South Bohemia, 370 05 České Budějovice, Czech Republic*
[6]*Czech University of Life Sciences, 165 00 Prague, Czech Republic*
[7]*University of Alberta, Edmonton T6G 2E3, Alberta, Canada*
e-mail: daniel.petras@geology.cz

ABSTRACT: **Lake Medard (LM), a post-mining lake in the Czech Republic with stratified, sulfate- and iron-rich bottom waters, serves as a natural laboratory to study sediment–water-interface (SWI) dynamics where steep aqueous redox gradients are present. This study investigates the interplay of redox conditions, microbial activity, and sedimentary processes, revealing that short-term Eh fluctuations (80–100 mV) in the bottom water significantly mobilize rare earth elements (REE) and influence the partitioning of other redox-sensitive elements such as vanadium (V) and arsenic (As) from reactive iron (Fe)- and manganese (Mn)-oxyhydroxides during early diagenesis. While carbonate phases like siderite primarily retain their REE signatures, they can incorporate REE released during these redox shifts. Spectroscopic analyses confirms the presence of FeOOH polymorphs (goethite and lepidocrocite) in organo-mineral aggregates in the upper sediments. Sequential extractions shows that under stronger reducing conditions (Eh ≈ –190 mV), As predominantly associates with carbonates, shifting to Fe(III)-oxyhydroxides at higher Eh (≈ –80 mV). Isotope analyses ($\delta^{13}C$) indicate that the bulk sediment carbonate is detrital, sourced from Miocene strata. Authigenic pyrite in LM sediments exhibits $\delta^{34}S_{py}$ values (–35.1 to –23.0‰), reflecting microbial sulfate reduction. However, the accumulation of the byproduct sulfide, and thus pyrite stabilization, is limited by the low availability of labile organic substrates and the reoxidation of sulfide by Fe(III)-oxyhydroxides. These findings highlight the sensitivity of geochemical signals in sediments to subtle redox shifts and improve our interpretation of ancient deposits formed under dynamic water column redox conditions.**

INTRODUCTION

Lake Medard, a post-mining lake in the Czech Republic (Fig. 1), has been proposed as a natural laboratory for studying dynamic redox conditions and mineralogical transformations driven by aqueous biogeochemical processes (Petrash et al. 2022). It may also provide valuable insights for designing bioreactors optimized for secondary metal recovery (Valdés et al. 2024). This recently made, out-of-equilibrium lake—a former lignite mine filled with diverted river water currently features a density-stratified bottom water column with well-defined redox gradients. At water depths ≥ 48 meters below the lake surface (m.b.l.s.), dissolved oxygen (O_2) becomes depleted and the system transitions to an anoxic, ferruginous and sulfatic state characterized by dissolved ferrous iron (dFe^{2+}) ≥10 μM and dissolved sulfate (dSO_4^{2-}) ≥1000 μM. This redox structure is unusual in natural ferruginous lakes, and results from low water nutrient contents (oligotrophic state) influencing the development of distinct hydrochemical zones, each hosting substantial chemolithotrophic proteobacterial communities driving vigorous biogeochemical elemental cycling (Petrash et al. 2018, 2022). Despite the high dSO_4^{2-}, microbial sulfate reduction (MSR)—a major anaerobic respiration process—is not a dominant pathway in the lake bottom waters, and dissolved sulfide (H_2S) does not accumulate (≤ 0.25 μM; Petrash et al. 2018). Instead, a delicate balance between microbial metabolisms, including Mn, Fe, and S respiration, dictates the prevailing aqueous biogeochemistry (Valero et al. 2024).

Studies of modern redox-stratified lacustrine systems integrating gene sequencing, isotope analyses, and sediment mineralogy have validated the reliability of several emerging isotope proxies increasingly being used to reconstruct past environmental conditions (e.g., Wirth et al. 2013). Such a combined approach has confirmed that lacustrine sediments can function as geobiological archives, capturing key geochemical and biological processes prevailing at the time of deposition, mineral authigenesis, and/or early diagenetic alteration (Havas et al. 2025). However, the extent to which minor postdepositional redox fluctuations in the overlying water column influence commonly used bulk sedimentary proxy records—such as shale-normalized cerium (Ce) anomalies (Lau and Hardisty 2022; Zhang and Shields 2022) and relative enrichments in V (Algeo and Liu 2020) and/or

Published Online: August 2025
 1527-1404/25/095-707

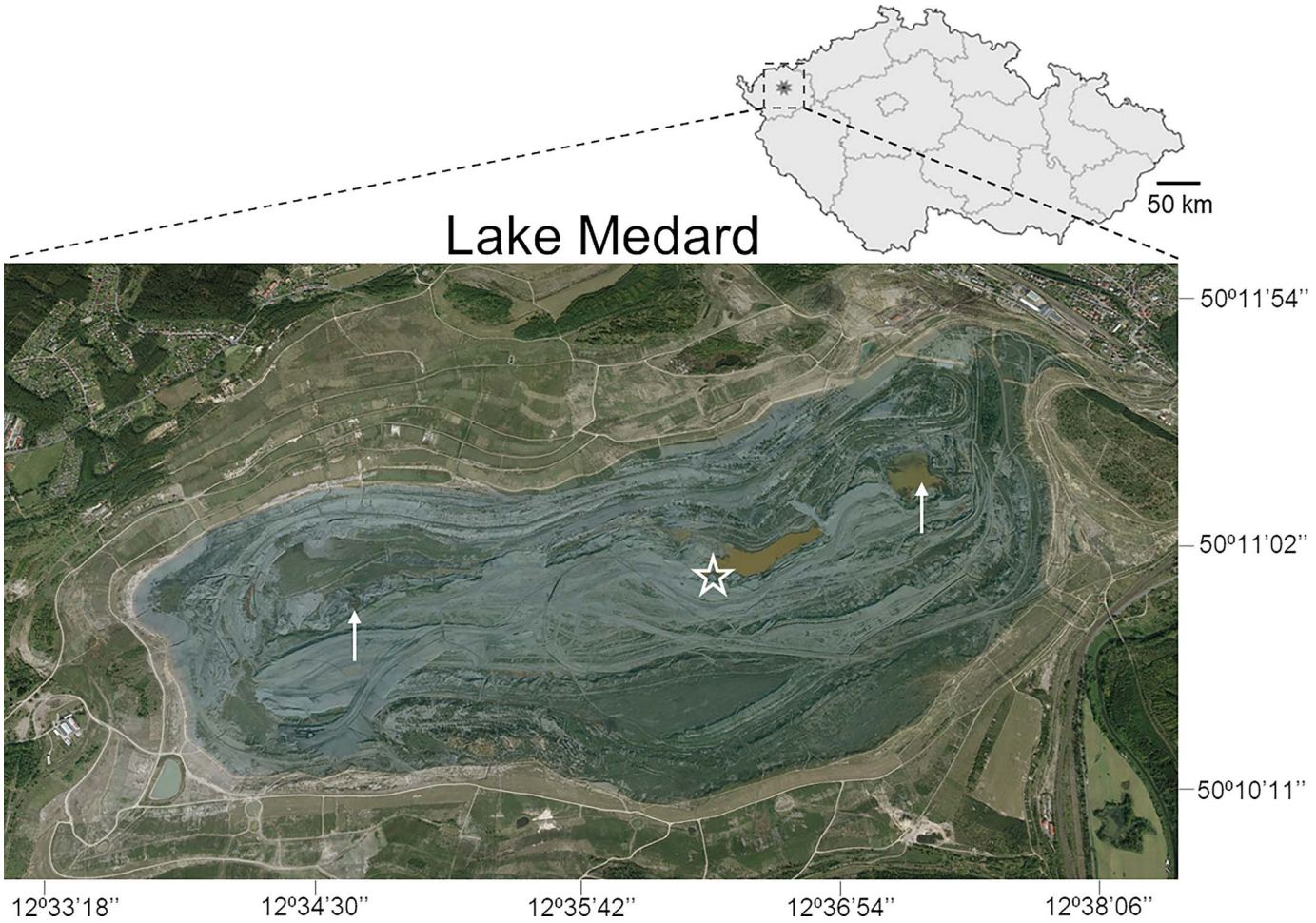

FIG. 1.—Lake Medard in NW Czech Republic. The current aerial extent of LM is superimposed on the former Landsat imagery of the abandoned mine pit from Jan. 2004 (© GEODIS Brno). Star marks the central sampling location at coordinates 50°10′45″ N, 12°35′45″ E. The approximate locations of the other two depocenters mentioned in the text are also shown (arrows).

As (Tribovillard 2020) during mineralogical alteration and stabilization—remains uncertain.

In Lake Medard (hereafter LM), the presence of redeposited siderite and the fluxes of dissolved inorganic carbon ($HCO_3^- + CO_3^{2-}$) exert a buffering role, and the speciation of redox-sensitive elements like As, V, and REE appears to be substantially impacted by the reactivity of detrital and authigenic carbonates in the upper sediment (Umbría-Salinas et al. 2021), while electron transfer processes involving iron mineral aggregates formed in the water column and interacting with planktonic bacteria appears to exert a role in the internal cycling of As (Valero et al. 2023) and REE (Váldes et al. 2024).

This study integrates spectroscopic, isotopic, and mineralogical data from the bottom waters of Lake Medard and its recent sedimentary pile to investigate how aqueous redox variability influences sedimentary geochemistry. Solid-phase analyses were conducted using powder X-ray diffraction (XRD), while Fe_{K1}-edge X-ray absorption spectroscopy (XAS) was used to elucidate the local atomic environment of Fe atoms. Elemental concentrations were determined through a sequential extraction scheme calibrated for reactive iron-bearing minerals, followed by mass spectrometry of each of the extracted fractions (Clarkson et al. 2014). Collectively, these methods provide a detailed characterization of Fe(III)- and Mn(IV)-oxyhydroxides and carbonates as primary carrier phases for REE, As, and V. Their contents in LM sediments were evaluated over two sampling campaigns during which a ±100 mV fluctuation in Eh was documented in the bottom water column. These phases therefore serve as proxies for assessing the impact of transient redox shifts on sedimentary records. Figure 2 illustrates the multi-analytical, multi-phase, and multi-sampling approach used in this study.

The dissolution and reprecipitation of minerals at the SWI of LM was found to exhibit complex interactions between redox dynamics, microbial activity, and sedimentary processes. Our findings highlight the susceptibility of REE in reactive Fe(III)- and Mn(IV)-oxyhydroxides to mobilization during early diagenesis, driven by short-term changes in Eh. Although carbonates such as siderite appear to retain their primary REE signatures, these reactive phases incorporate REE released into the pore waters during transient redox shifts. Microbial activity in the aqueous redox interface directly influences the redox state of the upper sediment, which in turn dictates the stability of minerals like Fe(III)- and Mn(IV)-oxyhydroxides, and their interaction with carbonates in the clayey matrix. Tanden mineral dissolution–precipitation releases REE, As, and V in the porewaters, which can then be differentially re-complexed by other reactive sedimentary phases. This continuum influences bulk-sediment chemistry and has a subsequent impact on the element distribution (partitioning) in diagenetically altered phases. The implications of this research extend beyond the studied system, providing a framework for interpreting ancient sediments deposited and altered under dynamic redox conditions. By examining these processes in a recently formed lake system, we aim to enhance the reliability of the use of sedimentary geochemical proxies and refine our understanding of past environmental conditions.

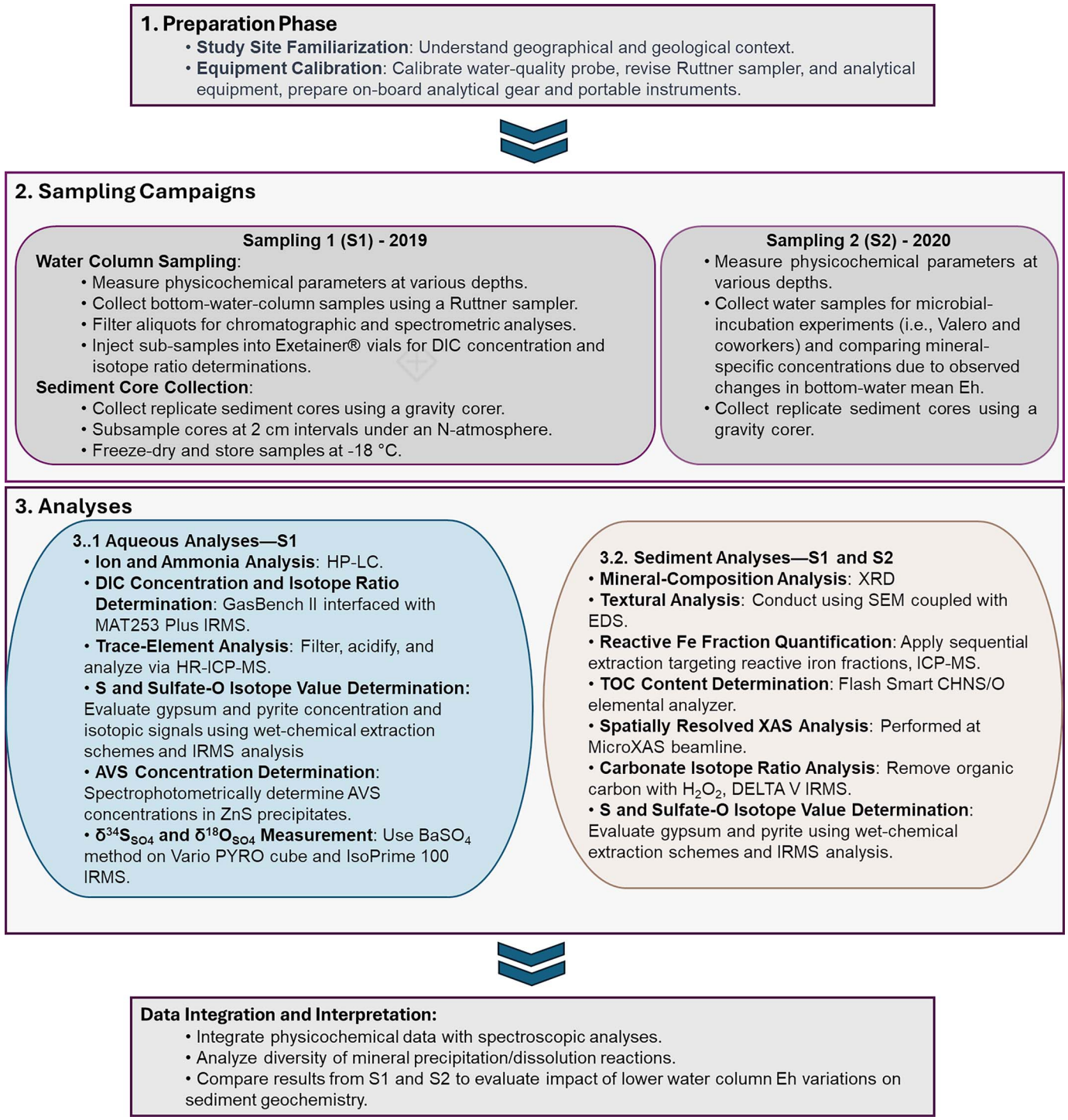

FIG. 2.—Schematic overview of the multi-analytical, multiphase, and multi-sampling approach used in this study, summarizing the methodologies applied and their respective targets.

STUDY SITE

Located in the Sokolov mining district, approximately 19 km west-southwest of Karlovy Vary, Czech Republic, LM was formed through the reclamation of the decommissioned Medard–Libík open-cast lignite mine. The lake was generated by diverting water from the nearby Eger (Ohře) river into the opencast pit, and now it spans an area of 4.9 km^2. It reaches maximum depths between 48 and 60 m.b.l.s. in three depocenters, which correspond to the deepest areas of the former pit (Fig. 1).

During the mid 2000s closure and abandonment stage of the mine, Fe and SO_4^{2-}, derived from the oxidation of sedimentary pyrite in the mine overburden, leached into shallow pit lakes that formed from infilling groundwater (Murad and Rojík 2003, 2005). The hydrochemistry of those shallow pit lakes was further influenced by runoff carrying particles and

solutes from weathered Miocene tuffaceous and carbonate-rich claystone in the mine overburden. These claystone deposits are from a Burdigalian rift lake (Rojík 2004). Authigenic minerals that accumulated in the early formed acidic shallow pit lakes included two-line ferrihydrite, schwertmannite, goethite, and jarosite, along with detrital minerals such as kaolinite and muscovite, both of which are abundant in the Miocene overburden (Murad and Rojík 2003). These are common minerals that control major-ion and trace-metal solubility in pit lakes (Davis et al. 2024). There are also records of thenardite (Na_2SO_4) epifluorescences associated with faults and fractures (Šmejkal 1978; Kříbek et al. 2017).

The hydrochemistry of modern LM is influenced by groundwater–rock interactions, eolian deposition, ongoing mineral transformations of the former mine spoils, and weathered Miocene detritus redeposited in the lakebed during water infilling (Petrash et al. 2022). The bedrock interacting with groundwater fluids contains weathered pyritic coal seams and carbonate (dolomite and/or siderite)-cemented claystone layers. A layer containing abundant greigite is at approximately 55–58 m below the surface (Krs et al. 1990; Kříbek et al. 2017). The basement rocks are mostly granitoids, but alkaline basaltic volcanics also influence regional sedimentation in the rift basin (Rojík 2004; Rapprich et al. 2023). The claystone-embedded lignite, mined on-site before exhaustion since the early 20th century, is known for having concentrations of lanthanides and As higher than global averages (Bouška and Pešek 1999). The depocenter of the lake currently exhibits a meromictic structure (i.e., a persistently stratified water column), providing valuable insights into biogeochemical interactions, including the dissolution and coprecipitation of metastable minerals mediated by chemolithotrophic prokaryotes. The modern post-mining lake sediments are comparatively enriched with lanthanides and As (Umbría-Salinas et al. 2021).

MATERIALS AND METHODS

Water-Column Characterization (Pre-Sampling).—Aqueous physicochemical parameters were measured using a YSI 6600 V2-2 water-quality probe (Xylem Analytics). Conductivity, temperature, O_2, pH, and Eh were simultaneously measured at depths ranging from 47 to 55 m in central LM (Fig. 1). This water monitoring design aimed to understand the physicochemical properties of the bottom lake waters before water sampling. Probe measurements had a 1-m resolution above and below the O_2 minimum zone, and 0.5 m at the chemocline. During sampling, the chemocline was at approximately 48 m.b.l.s. (Fig. 3). Accordingly, sampled depths were 47, 48, 48.5, 49, 50, 52, 54, and 55 m.b.l.s., with replicates at 47, 48.5, 50, and 54 m.b.l.s.

Sampling.—Bottom-water-column samples ($N = 8$, four replicates) were collected in November 2019 (Sampling 1, S_1) using a Ruttner sampler with 1.7 L capacity, ensuring thorough dH_2O flushing between samples. Onboard, water-sample aliquots (both acidified and non-acidified) were filtered using high-flow 28 mm diameter polyether-sulfone filters with a 0.22 μm cut-off for various chromatographic and spectrometric analyses. For determination of concentrations of dissolved inorganic carbon (DIC) and its $^{13}C/^{12}C$ isotope ratio, subsamples were injected into sealed Exetainer® vials containing H_3PO_4 and He(g) headspace immediately upon sampler retrieval to the vessel.

Replicate sediment cores were collected using a messenger-activated gravity corer and analyzed for mineralogy down to 8 cm below the SWI. Cores were subsampled at 2 cm intervals in a custom-made glovebox under an N-atmosphere. Samples were immediately frozen using liquid N and then freeze-dried before being stored at –18°C until further analyses. A second sediment sampling (Sampling 2, S2) was conducted at the same location in early December 2020, following an observed shift in bottom-water mean Eh from approximately –210 mV (S1) to –80 mV (S2). This shift was measured in the bottom water column at hypolimnial depths of the central sampling location, as marked in Figure 1. Although the primary aim of the second sampling campaign was to collect samples for experiments on microbial incubation, it also targeted the sediments to compare mineral-specific concentrations of V, As, and REE contents. This allows for the evaluation of how short-term variations in Eh in the lower water column affect the geochemistry of the upper sediment.

Aqueous Analyses.—We integrated physicochemical data with spectroscopic analyses of the bottom water column, including concentrations of dissolved ions, volatile fatty acids, $\delta^{34}S$ and $\delta^{18}O$ isotope ratios of dSO_4^{2-}, determinations of DIC concentrations, and $\delta^{13}C_{DIC}$. The analyses provide insight into the diversity of mineral precipitation–dissolution reactions occurring in the bottom water column of LM. These reactions affect the delivery of reactants and influence their early diagenetic transformation of minerals at the SWI.

Ions and ammonia were analyzed using high-performance liquid chromatography, HP-LC (ICS5000 + Dionex) with IonPac AS11-HC-4 μm and CS16-4 μm columns, achieving recoveries exceeding 80%. The determination of ion concentrations have a 2σ error $< 20\%$ based on analytical replicates.

DIC concentrations and isotope ratios were analyzed using a GasBench II peripheral interfaced with a MAT253 Plus IRMS. DIC concentrations were determined by stripping the evolved gas and measuring the total CO_2 contents and their isotope ratios using a Conflo IV device (Thermo Scientific). Errors in concentration measurements were $< \pm 4\%$, with $\delta^{13}C_{DIC}$ values normalized to IAEA-603, achieving reproducibility of $< \pm 0.05‰$.

Water samples (15 mL) were filtered through 0.22 μm PES filters, acidified on-site, and subsequently analyzed via HR-ICP-MS (Thermo Element2) back in the laboratory. Calibration was performed using multi-element standards (0.5, 5, 50 ppb) and Indium (5 ppb) for drift correction. Detection limits were < 0.01 wt. % for Fe and Mn, and 0.001–0.002% for potassium (K), sodium (Na), magnesium (Mg), and calcium (Ca). The instrument was tuned to minimize oxide production, and solutions of praseodymium (Pr)-neodymium (Nd), barium (Ba)-Ce, and samarium (Sm)-terbium (Tb) were analyzed to quantify potential oxide interferences, which were found to be negligible. Calibration against multi-element solutions ensured accuracy better than 5% for REE and 10% for other elements.

Concentrations of acid volatile sulfur (AVS) were determined spectrophotometrically in ZnS precipitates following the methods described by Rice et al. (1993). $\delta^{34}S_{SO4}$ and $\delta^{18}O_{SO4}$ were measured using the $BaSO_4$ method on a Vario PYRO cube (Elementar) and IsoPrime 100 IRMS. The protocol involved acidifying 10 to 30 mL of sample water to pH 2 with 4N HCl ($\sim$ 200–300 μL), then mixing with 1M $BaCl_2{\cdot}2H_2O$ solution (pH 2) in centrifuge tubes. The mixture was heated and agitated at 75°C for one hour, followed by multiple centrifugation and rinsing cycles with deionized water. The recovered $BaSO_4$ powder was dried at 50°C overnight. Each purified $BaSO_4$ sample was analyzed for $\delta^{34}S_{SO4}$ and $\delta^{18}O_{SO4}$, with analytical errors of $\pm$ 0.4‰ (2σ) and reproducibility $< 0.3‰$ (1σ). Isotope values were normalized to the NBS 127 standard, with a $\delta^{34}S$ value of +20.3‰ (VCDT scale) and $\delta^{18}O$ value of +9.3‰ (VSMOW scale), achieving an average analytical reproducibility of $\pm$ 0.5‰.

Using our physicochemical data, and pertinent measured elemental concentration determinations, we conducted calculations of aqueous-mineral equilibrium to determine the potential for relevant minerals to precipitate from the overlying water column. These were conducted using the USGS geochemical equilibrium modeling software PHREEQC (Parkhurst and Appelo 1999), which permits deriving theoretical speciation results that can be presented in terms of the saturation index (SI) for predicted minerals, where SI is defined by $SI = \log (IAP/K_{sp})$, with IAP and K_{sp} being the ion activity product of the dissolved constituents and solubility product for the minerals considered. The equilibrium constants and solubility product constants were taken from the WATEQ4f database, which is part of the PHREEQC download package.

Sediment Analyses.—Mineral composition was determined semiquantitatively via powder XRD using a Bruker D8 Advance powder diffractometer

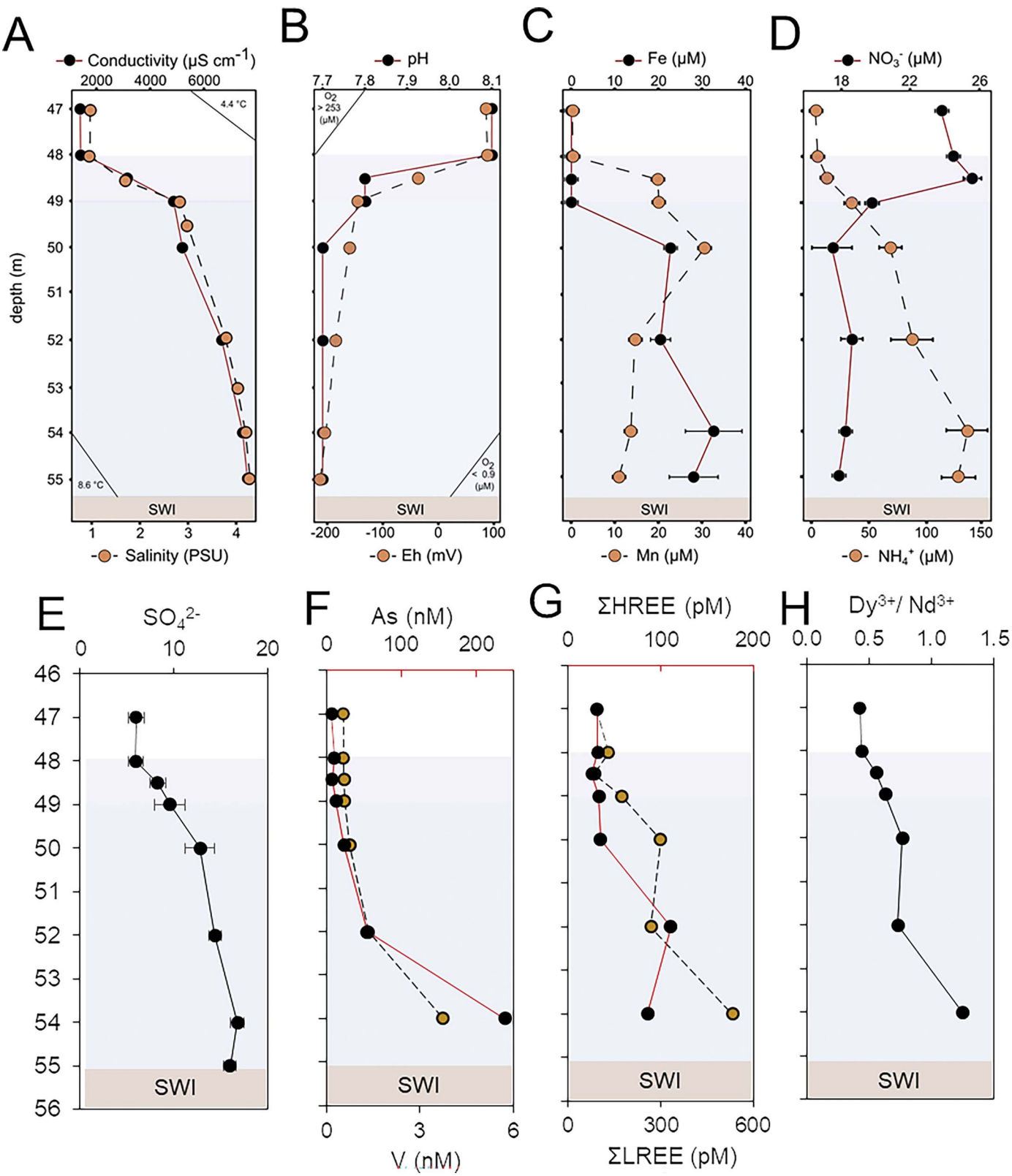

FIG. 3.—Redox-driven solubility and mobility patterns in LM's bottom water column. **A**, **B)** Profiles of conductivity, temperature pH, Eh, and dissolved O_2 showing variability of measured parameters with increasing water column depth (m.b.l.s.). **C)** Profiles of dFe^{2+} and dMn^{2+}. **D)** Counter-gradients of nitrate and ammonium concentrations. **E)** Profiles of dissolved iron and sulfate; a concurrent decrease of both $dSO4^{2-}$ and dFe^{2+} suggests FeS precipitation by the SWI. **F)** Increasing trends in dissolved As and V concentrations with increasing depth. **G**, **H)** Concentration profiles of the sums of LREE and HREE illustrate the dynamics of reductive dissolution and subsequent re-complexation processes affecting lanthanide partitioning in the water column. This is better exemplified by the molar ratio of Dy/Nd for HREE and LREE, respectively.

using Bragg-Brentano geometry, and 40 kV CuKα radiation (λ = 1.54058 Å), with corrections for preferred orientation of K-feldspars and micas. XRD data were collected over a 2θ range of 4 to 80°, with 0.015° step increments and 0.8 s per step. Textural analyses of sediments were conducted using either a MAGELLAN 400 scanning electron Microscope (SEM) coupled with an Apollo X Si drift detector for X-ray microanalysis, or a TESCAN Mira 3 Field Emission SEM coupled with an Oxford Nano energy-dispersive X-ray spectrometer.

To quantify reactive Fe fractions, we applied a sequential extraction targeting the reactive pool of iron that is susceptible to reductive dissolution by H_2S (Poulton and Canfield 2005). For each sediment layer sampled, 100 mg aliquots were subjected to a multistep chemical leaching procedure targeting sodium acetate-soluble Fe, dithionite-soluble Fe oxides, oxalate-soluble Fe, and pyrite (after Poulton and Canfield 2005; Clarkson et al. 2014). Any remaining phases after leaching, presumably silicates, were considered inert in response to dissolved H_2S within the time frame relevant to the diagenetic alteration of the post-mining lake sediments studied here (Raiswell et al. 2018). This scheme allows for the geochemical distribution of metal(loid)s to be discerned as follows: i) those associated with carbonate minerals, ii) those in easily reducible, poorly crystalline Fe-oxyhydroxides, iii) those in reducible, crystalline Fe-oxyhydroxides, and iv) pyrite. The Fe, Mn, V, As, and lanthanide concentrations of the extracts were determined using ICP-MS (Xseries II, Thermo Scientific). Indium (^{115}In) at a concentration of 1 μg L^{-1} was used as an internal standard. To optimize the analysis for REE, the instrument was calibrated to maintain a CeO/Ce ratio below 1.5%. A five-point calibration curve was established using dilutions of single-element standards Certipur® and REE mix TraceCERT®, at concentrations ranging from 0 to 50 μg L^{-1}. The precision of the elemental concentration data was established to be ≥ 90% based on the analysis of replicate samples.

Contents of total organic carbon (TOC) were determined using a Flash Smart (Thermo Fisher Scientific) CHNS/O elemental analyzer. The bulk-rock mineral composition was determined semiquantitatively via XRD using a D8 Advance powder diffractometer. In addition, spatially resolved X-ray absorption (XAS) analyses were performed at the MicroXAS beamline at the Swiss Light Source. For XAS, the incident beam was focused to a size of approximately 1 μm × 1 μm using a Kirkpatrick-Baez (KB) mirror system. X-ray-fluorescence (XRF) experiments were run on a monolayer of fine sediment particles (< 2 μm) attached to Kapton tape to locate analytical areas exhibiting Fe hotspots. The transmitted signal was collected using a standard silicon diode, while the fluorescence signal was detected with a single-element Si detector (Ketek) mounted at a 90° angle to the incident beam. The energy of the X-ray beam was adjusted using a fixed-exit monochromator equipped with a pair of Si (111) crystals. Iron coordination and redox state were investigated through X-ray absorption near-edge structure (XANES) spectroscopy with the beam tuned slightly above the Fe K-edge.

For XANES analysis, the X-ray energy was calibrated using Fe foil as a standard, setting the centroid of the pre-edge peak maximum (1st inflection point) to 7112.1 eV. The acquisition time of ~ 20 min per scan, with three scans per region of interest (Fe hotspot) was determined using XRF maps (not shown). Spectra from samples were fitted with linear combinations of component spectra using a non linear least-squares algorithm implemented in Athena (Ravel and Newville 2005). During data processing in Athena, spectra were aligned to a common energy scale by setting the first inflection point of the first derivative to 7126.3 eV (corresponding to the energy at half the step size) of reference. The experimental spectra of the measured samples were then adjusted to account for any observed shifts in absorption energy. A principal component analysis of Fe_{K1}-edge, k2-weighted average XANES spectra was obtained. The approach weighs these components as a function of their ability to reconstruct the features (minus noise) of the sampled spectra.

The isotope ratios of carbonates in the sediment fraction were analyzed following the removal of organic carbon with hydrogen peroxide (H_2O_2), using the method described by Rosenbaum and Sheppard (1986). These ratios were measured using a DELTA V mass spectrometer (Thermo Fisher Scientific), coupled with an EA-1108 elemental analyzer (Fisons) and a ConFlo IV reference gas interface. The isotope composition of sedimentary organic carbon, $\delta^{13}C_{org}$, was measured using the same instrument. For this purpose, finely milled samples were placed in tin capsules and oxidized to CO_2 at 1040°C in the elemental analyzer. Measurement accuracy for siderite samples was assessed using the IAEA NBS-18 standard (certified values: $\delta^{13}C = -5.01‰$, $\delta^{18}O = -23.2‰$) and two in-house standards. Results were consistent with the certified values. Long-term laboratory reproducibility was better than 0.05‰ for $\delta^{13}C$ and 0.1‰ for $\delta^{18}O$. Additionally, the NBS-22 reference material ($\delta^{13}C = -30.06‰$, US National Bureau of Standards) was analyzed to verify measurement accuracy, achieving a reproducibility better than 0.12‰.

Stable-isotope analyses were conducted to determine sulfate S and O isotope values for gypsum ($\delta^{34}S_{gy}$ and $\delta^{18}O_{gy}$), and chrome-reducible sulfur ($\delta^{34}S_{CRS}$) for pyrite. To evaluate $\delta^{34}S_{gy}$, the heavy-mineral fraction, including pyrite, was excluded using 1,1,2,2-tetrabromoethane (ρ = 2.95). Gypsum was then dissolved in ddH_2O to extract sulfate, which was later precipitated as $BaSO_4$ (as described above). The $BaSO_4$ was converted to SO_2 by direct decomposition with V_2O_5 and SiO_2 powder and combusted at 1000°C under vacuum (10^{-2}–10^{-3} mbar). The evolved SO_2 was analyzed using a Finnigan MAT 251 IRMS dedicated to S isotope determinations. The results are expressed in delta notation and reported against the VCDT and VSMOW standards, with an accuracy determined through international standards and reproducibility better than 0.2‰. The IRMS instrument used for dSO_4^{2-} isotope ratios was also used to determine the $\delta^{34}S$ of pyrite in the upper sediments. Before analyses, an AVS/CRS wet-chemical extraction scheme was applied (Thomazo et al. 2019, for details). After centrifugation, the Ag_2S precipitate was washed with ddH_2O and oven-dried at 50°C for 48 h. Pyrite S isotope measurements ($\delta^{34}S_{py} \equiv \delta^{34}S_{CRS}$) were performed on SO_2 molecules by combusting ~ 500 mg of silver sulfide mixed with WO_3 using the Vario PYRO cube (Elementar) instrument described above. Calibration was performed using international standards (IAEA-S-1, IAEA-S-2, IAEA-S-3), with analytical reproducibility better than 0.5‰ based on replicates for standard materials and samples.

RESULTS

Elemental Cycling in the Water Column and Sources

Water-Column Structure and Redox Potential Dynamics.—The water column of LM is stratified (Fig. 3; see Boehrer and Schultze 2008). The epilimnion at the sampled depths is principally defined by its conductivity (≤ 900 μS cm^{-1}; Fig. 3A) and extends from the lake surface to depths of between 44 and 48 m.b.l.s in LM's western and central depocenters, respectively. Density stratification, denoted by steep gradients in conductivity (and salinity; Fig. 3A), generates a permanent chemical boundary zone, i.e., the chemocline, which separates the oxygenated and seasonally mixed epilimnion from the hypolimnion. A pH gradient, ranging from alkaline to circumneutral (8.2 to 7.4), was observed, decreasing with increasing water depth (Fig. 3B). The hypolimnion (≥ 49 m.b.l.s.) is characterized by marked O_2, pH, Eh, and temperature gradients (Fig. 3B; Table S1).

Our winter monitoring campaigns (this study) revealed an inverted thermocline, where temperature increases with depth due to surface cooling and the presence of a denser water mass towards the SWI (Fig. 3A). In summer (cf. Petrash et al. 2018), the thermocline consists of warmer water above cooler, denser bottom waters. At about 54 m.b.l.s. and approximately 2 m above the SWI at the sampling site (Fig. 1), the hypolimnion features O_2 levels below the detection limit (DL) of the probe (Fig. 3B). This characteristic is well established in the central and western depocenters of LM. However, in the eastern part of the lake, hypoxic, sulfatic groundwater recharge events may result in the temporal disappearance of the hypolimnial O_2-depleted zone (Petrash et al. 2018, 2022). The temporally and laterally

TABLE 1.—*Dissolved concentrations of manganese, iron, inorganic carbon (i.e., DIC = measured as HCO_3^-) and sulfate (and their measured isotope values), and reactive nitrogen species (nitrate (NO_3^-) and ammonia (NO_4^+)) at the central deepest part of LM water column (47 to 55 m depth below the surface). The corresponding physicochemical parameters and dissolved trace metal contents pertaining the sampled bottom water column are shown in Supplemental Table SM1.*

Depth (m)	Mn^{2+} (μM)	Fe^{2+} (μM)	DIC (mM)	$\delta^{13}C$ (‰)$_{VPDB}$	SO_4^{2-} (mM)	$\delta^{34}S$–SO_4^{2-} (‰)$_{VCDT}$	$\delta^{18}O$–SO_4^{2-} (‰)$_{VSMOW}$	NO_3^- μM	NH_4^+ μM
47	0.33 ± 0.01	0.07 ± 0.01	nd.	nd.	6.00 ± 0.80	+10.90 ± 0.10	nd.	23.80 ± 0.50	3.40 ± 0.40
48	0.42 ± 0.01	0.07 ± 0.01	1.90 ± 0.10	+0.20 ± 0.05	5.90 ± 0.80	+13.50 ± 0.07	+13.20 ± 0.20	24.50 ± 0.50	5.20 ± 0.50
48.5	19.92 ± 0.36	0.07 ± 0.01	3.50 ± 0.20	–0.10 ± 0.05	8.30 ± 0.80	+11.30 ± 0.03	+13.10 ± 0.05	26.00 ± 0.50	15.40 ± 0.50
49	20.11 ± 0.36	0.07 ± 0.01	7.50 ± 0.10	–2.10 ± 0.03	9.60 ± 1.60	+11.50 ± 0.10	+14.20 ± 0.10	19.80 ± 1.20	34.50 ± 9.30
50	30.57 ± 0.55	22.80 ± 0.40	5.90 ± 0.10	–2.70 ± 0.10	12.80 ± 1.60	+12.10 ± 0.10	+12.70 ± 0.40	17.50 ± 1.20	68.70 ± 9.30
52	14.62 ± 0.26	20.50 ± 2.30	9.80 ± 0.20	–2.50 ± 0.10	14.40 ± 0.70	+12.50 ± 0.10	+13.80 ± 0.20	18.70 ± 0.20	87.30 ± 14.70
54	13.72 ± 0.25	32.70 ± 6.50	9.00 ± 0.20	–3.90 ± 0.40	16.80 ± 0.70	+13.30 ± 0.10	+13.20 ± 1.10	18.30 ± 0.20	134.50 ± 14.70
55	11.08 ± 0.20	28.10 ± 5.60	nd.	nd.	16.00 ± 0.70	nd.	nd.	17.90 ± 0.20	127.70 ± 14.70

nd.: Not determined.

variable redox structure of the newly formed water body has been observed since early stages of water infilling (Vrzal et al. 2011).

At the central sampling location (Fig. 1), we documented a temporary shift in the hypolimnial Eh from the more prevalent ca. –210 mV to –80 mV. The chemocline depth shifted from 48 m (S_1) to 52 m (S_2). This shift was linked to a 77% decrease in precipitation before our sampling, as recorded by the Czech Hydrometeorological Institute (https://www.chmi.cz/historicka-data/pocasi/uzemni-srazky?l=en). Near the SWI, water conductivity dropped from 6,808 μS cm^{-1} (in S_1, Nov. 2019) to 2,607 μS cm^{-1} (S_2, Dec. 2020). Physicochemical conditions in the water column reverted to S_1-like parameters as observed about five months after S_2 (Umbría-Salinas et al. 2021).

The hypolimnion of LM is ferruginous, manganous, and nitrogenous. The concentration profiles of dissolved Mn^{2+} and Fe^{2+} have similar peak values, about 31 μM, but exhibit differences across the chemocline (Fig. 3C, D; Table 1). The peak in Mn^{2+} concentration likely coincides with zones where Mn(IV) oxyhydroxides can be reductively dissolved in association with dFe^{2+} oxidation (Davison 1993; Lovley and Phillips 1988). From this point source of dMn^{2+}, located in the water column at about 50 m.b.l.s. (Fig. 3D), Mn^{2+} concentrations decrease downward, which suggest recomplexation and/or coprecipitation with multi-valent oxyhydroxides-bearing particulates formed at the chemocline and partially stabilized in transit to the SWI. We refer to these particulate to as "iron snow" (Reiche et al. 2011).While these particulates were not directly sampled in this study, their formation at the chemocline is inferred from the fact that upon retrieval of water samples from below the chemocline, rapid oxidation of dFe^{2+} upon exposure of the sampler contents to pO_2 leads to the formation of readily visible particles, turning the previously clear water in the sampler cloudy and reddish.

Nanoparticles of Fe(III) oxyhydroxides are known to form under conditions of high supersaturation (such as those observed below the chemocline, where dFe^{2+} concentrations are increased, indicating progressive reductive dissolution and/or respiration of Fe(III)-bearing phases in iron snow (e.g., Raiswell and Canfield 2012, their SI-3). This inference is supported by counter gradients of reactive N species in the water column, which indicate active N cycling (with dFe^{2+}). The development of a plateau in ammonium (NH_4^+) concentrations in the hypolimnion is accompanied by a sharp decline in nitrate (NO_3^-) at the chemocline (Fig. 3D; Table 1). Farther down the water column, near the SWI, a moderate decrease in Fe^{2+} might reflect reprecipitation with by-product sulfide, known to be present near the SWI at sub-μM concentrations (see below). At this level, the relative abundance of microbes capable of sulfate reduction increases slightly (Petrash et al. 2022).

A distinctive feature of LM's bottom waters is their relatively dSO_4^{2-} concentrations, which increase with depth and range from 5.2 to 17.5 mM, with a 0.8 mM decrease in dSO_4^{2-} levels near the SWI (Fig. 3E). The concentration profiles of dSO_4^{2-} in the water column, similar to those of transition metals (Fig. 3C, E; Table 1) exhibit lateral variations in their water-column contents. Inputs of dFe^{2+} appear to be higher in the western depocenter, while dSO_4^{2-} levels are higher in the eastern depocenter. The laterally opposite decrease in dFe^{2+} and dSO_4^{2-} fluxes has been observed in multiple monitoring and sampling campaigns (Petrash et al. 2018, 2022).

Precipitation, stabilization, and reduction and remobilization in the water column of LM also play a major role in controlling gradients of dissolved-metal concentrations. Our data show that particulate Mn(IV)-oxyhydroxides exported from the oxic zone of the water column are readily reduced in transit to the lake floor (Fig. 3C), and/or associates with more stable Fe(III)-oxyhydroxides, giving rise to multivalent phases that constitute iron snow. The reactivity of metal oxyhydroxides in these aggregates can have an impact on the concentration of other elements in solution while in transit to the SWI (Fig. 3F–H; Table S3). Concentrations of redox-sensitive V and As also increase toward the SWI (Fig. 3F), whilst REE concentrations increase as a function of their variable interactions with colloids in the bottom part of the density- and redox-stratified water column (see Burdige 1993; Tostevin 2021).

At the SWI, the mobilization of REE is linked to the reductive dissolution of mineral carrier phases coupled to organic-matter degradation (Burdige 1993, see also Hatje et al. 2024). The upward diffusion of lanthanides across the LM bottom water column results in differential recomplexation with partially stabilized (i.e., selectively reduced) Fe(III)-bearing particulate matter (iron snow). Accordingly, in the water column, owing to their larger ionic radii and low occupancy of the 4*f* electron shell, light REE (LREE: lanthanum (La) through europium, Eu), which confer them a more electropositive nature, are more likely to participate in ionic bonding (Evans 2013; Hatje et al. 2024; Tostevin 2021) and can rapidly form complexes with partially stabilized (poorly) crystalline oxyhydroxides in settling iron snow. This substantially decreases their dissolved concentrations (Fig. 3G, H).

Meanwhile, the less abundant heavy REE (HREE: gadolinium (Gd) through lutetium (Lu)) remain in solution. HREE have smaller ionic radii and a higher proportion of unpaired 4*f* electrons, which confer increased ionization potential. As the HREE diffusive front reaches the chemocline, HREEs are recomplexed by amorphous, highly reactive Fe(III) oxyhydroxides (e.g., ferrihydrite) formed near the dysoxic chemocline, leading to substantial decrease in their concentrations in this part of the water column (Fig. 3G, H). Below we evaluate how vertical variation in this complexation dynamics—linked to shifts in the water column redox structure and governed by biogeochemical processes (Evans 2013)—possibly affects the partitioning of other elements in the sediments.

Upper-Sediment Mineralogy and Compositional Responses to Eh Dynamics

Sediment composition and dynamics of metal partitioning in the upper sediments were examined using a suite of X-ray analyses. XRD revealed a

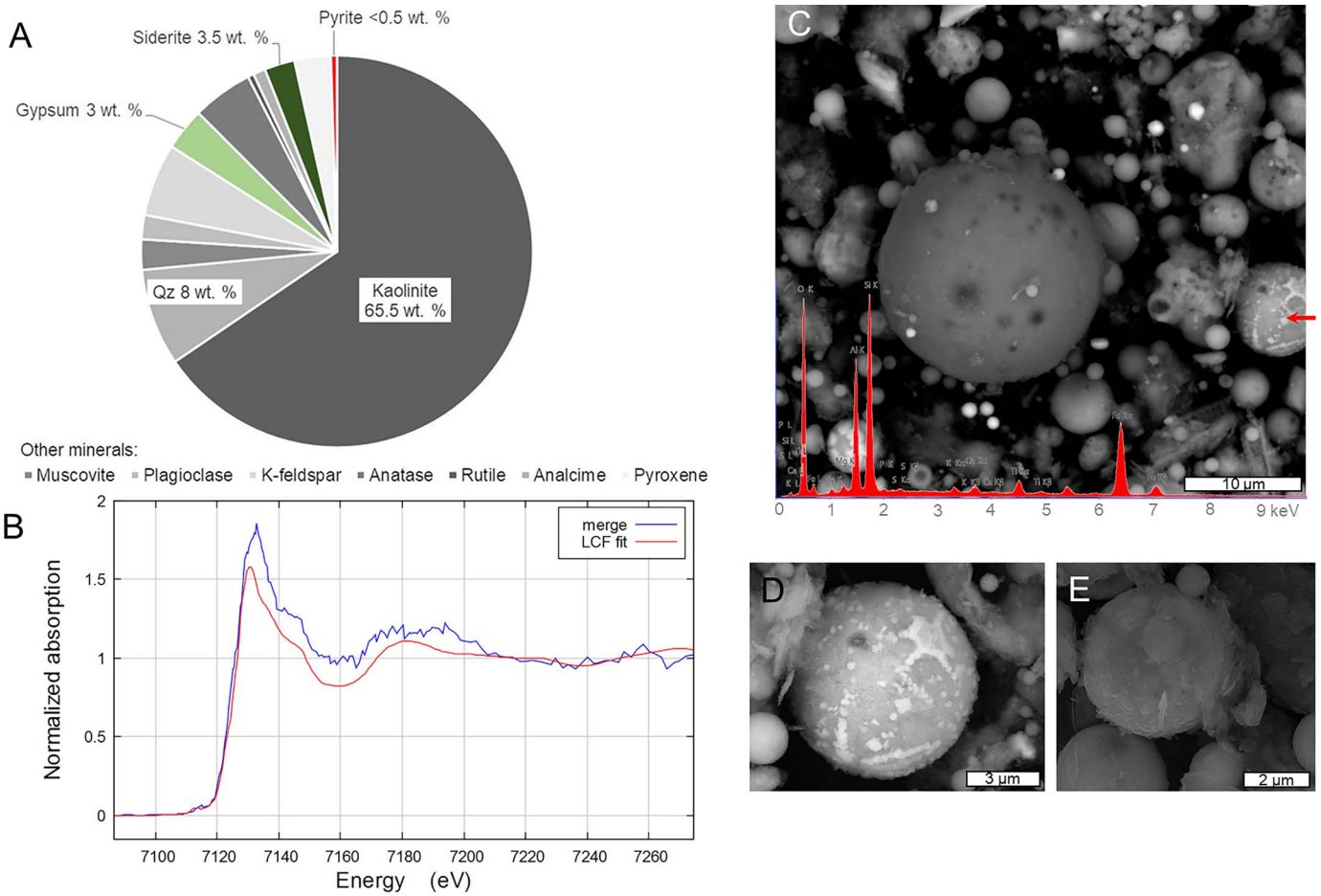

FIG. 4.—Sediment composition and metal partitioning dynamics in the upper sediments of Lake Medard. **A)** Semiquantitative XRD analysis revealing a sedimentary matrix composed predominantly of kaolinite, mica, and quartz, with minor constituents such as rutile, analcime, siderite, and gypsum (each 3–5 wt.%), and accessory pyrite (≤ 1 wt.%). Representative XRD of the sediments are in Figure SM1. **B)** Representative XANES analysis at the Fe_{K1}-edge indicating the presence of FeOOH polymorphs, notably goethite (α-FeOOH) and lepidocrocite (γ-FeOOH). The average three-measurements spectrum can be fitted (90 ± 4% fit) by two components in an octahedral coordination environment: goethite > lepidocrocite, which together account for 74–79% of the total variance in the Fe-bearing phases. An additional 21–26% is attributable to Fe(II)-bearing, mixed-valence hercynite ($Fe^{2+,3+}Al_2O_4$) clay as a third significant component. **C)** SEM images of organo-mineral aggregates in the upper sediment strata. The inset shows the particle electron dispersion spectrum, Fe high-intensity counts are attributed to Si and Al. **D**, **E)** Higher magnification SEM of the organo-mineral aggregates in backscatter and secondary electron imaging modes, respectively.

sedimentary matrix composed predominantly of kaolinite, mica, and quartz. In this clayey matrix are other minor constituents, such as rutile, analcime, siderite, and gypsum, each constituting approximately 3–5 wt.%. Accessory pyrite (≤ 1 wt.%) is also present (Fig. 4A). Representative powder XRD diffractograms are available in Figure SM1. The modern lake mineralogy closely resembles that observed in the Miocene lacustrine facies in the overburden of the former mine (Murad and Rojík 2003; Kříbek et al. 2017).

Calculations of aqueous-mineral equilibrium (Table 3) indicate the potential for some of the above-mentioned minerals to precipitate under the recorded pH, temperature, alkalinity, and ion concentrations (see Table 3 footnote). The equilibrium modeling revealed no substantial changes in the precipitation or dissolution potentials of sulfate- or iron-bearing species in the documented Eh-pH fields. This indicates that particulate-matter oxides and dSO_4^{2-} coexist in the hypolimnion. In the most reducing bottom waters, the equilibrium conditions can be conducive to the formation of pyrite precursors. Some of the phases predicted by mineral-equilibrium modeling, such as oxyhydroxides, were not detected via XRD (Fig. 4A, Fig. SM1). This is unsurprising given that powder XRD has a low sensitivity toward their poor crystallinity and/or the presence of the many interfering phases.

To spectroscopically assess LM oxyhydroxide contents, we used XANES at the Fe_{K1} edge (i.e., the characteristic X-ray absorption edge of Fe corresponding to the energy required to eject a 1s (K-shell) electron from an atom of iron). Its XAS position of the Fe_{K1} shifts slightly depending on the chemical environment and prevalent oxidation state of the iron (e.g., Fe^{2+} vs. Fe^{3+}) and the complexation environment. The results indicate the presence of FeOOH polymorphs, notably goethite and lepidocrocite (Fig. 4B). These phases comprise organo-mineral aggregates, as observed through SEM of the upper sediment strata (Fig. 4C–E).

Speciation Results.—As and V exhibit notably different partitioning behaviors in response to shifting redox conditions (Fig. 5A, B). Under a stronger redox gradient at the chemocline (S_1; Eh ≈ –190 mV), As associates predominantly with carbonates. However, as redox potentials increase (S_2; Eh ≈ –80 mV), As shifts toward preferential sorption on Fe(III)-oxyhydroxides—whereas V remains comparatively stable across these phases (Table 2). Distributions of lanthanide in the sediment pile offer insights into their mobility under oscillating redox states affecting reactive iron-bearing phases (Fig. 5A, B). In short-lived reducing episodes, Ce^{4+} initially adsorbed to Fe(III)- and Mn(IV)-oxyhydroxides undergoes

TABLE 2.—*Concentrations of Al, Fe (wt%), and Mn, V, As, the sum of lanthanides, and redox sensitive Ce (mg kg^{-1}), along with Ce anomalies (Ce*) in LM's anoxic sediment cores from 0 to 8 cm depth. These concentrations were determined after sequential extraction and spectroscopic analysis of the extracts. Sediment samples were collected under varying Eh conditions in the overlying bottom water column, specifically from monimolimnion layers at –180 and –90 mV. TOC values, exhibiting minor variability, are further detailed in the footnote of this table.*

Depth range (cm)	Fraction	Fe (wt. %)		Mn (mg kg^{-1})		V (mg kg^{-1})		As (mg kg^{-1})		ΣREE (mg kg^{-1})		Ce (mg kg^{-1})		Ce*	
		–190 mV	–80 mV	–190 mV	–80 mV	–190 mV	–80 mV	–190 mV	–80 mV	–190 mV	–80 mV	–190 mV	–80 mV	–190 mV	–80 mV
0–2	Carbonates	0.04	0.98	28.18	646.01	L.Q.	2.88	1.42	14.45	0.10	25.01	0.10	10.99	nd.	1.32
	Poorly crystalline oxyhydroxides	0.93	1.05	156.38	123.68	56.61	37.59	22.72	23.10	18.92	24.91	6.04	11.44	0.79	1.30
	Crystalline oxyhydroxides	0.45	0.10	26.95	4.63	11.70	67.84	18.50	L.Q.	9.87	L.Q.	1.15	L.Q.	0.45	nd.
2–4	Carbonates	1.17	1.02	74.46	321.63	43.14	10.10	17.64	7.71	28.26	27.14	9.01	11.81	0.79	1.29
	Poorly crystalline oxyhydroxides	0.79	1.07	126.43	112.12	46.36	35.26	16.58	18.17	27.00	26.51	8.81	12.92	0.77	1.92
	Crystalline oxyhydroxides	0.67	0.12	28.55	5.36	19.98	123.29	19.98	L.Q.	11.20	2.56	2.07	1.03	0.41	0.90
4–6	Carbonates	1.24	1.27	60.61	394.91	30.02	L.Q.	14.19	4.05	31.01	32.89	9.52	14.72	0.80	1.30
	Poorly crystalline oxyhydroxides	0.79	0.91	113.46	96.13	46.44	23.12	15.09	16.09	28.66	26.44	9.57	12.04	0.79	1.24
	Crystalline oxyhydroxides	0.67	0.07	28.18	4.48	20.69	47.48	19.34	L.Q.	13.75	2.33	2.53	0.79	0.49	0.71

TOC values decrease with increasing depth, remaining within the analytical error for both sediment sampling campaigns. They range from 5.1 ± 0.2 wt.% (at the SWI) to 3.7 ± 0.4 wt.% (at a sediment pile depth of 6–8 cm). The TOC predominantly consists of refractory lignitic particles. The repeatability of the core analyses, expressed as the relative standard deviation, varies for different elements. For V, Mn, and Fe, the repeatability ranges from 4.4% to 9.0%; for As, it ranges from 8.3% to 10.6%, and for REE, it ranges from 1.5% to 10.8%, all percentages being relative to the reported values. L.Q., less than the quantification limit.

TABLE 3.—*Saturation indices (log (IAP/K_{sp})) estimated for various minerals in theoretical equilibrium with LM's bottom water column at two distinct monimolimnial redox potentials (i.e., –190 and –80 mV).*

Mineral	SI*		Mineral	SI	
	–190 mV	–80 mV		–190 mV	–80 mV
$Al(OH)_3$ (am)	0.786	0.328	Huntite	–0.205	0.597
Al_2O_3(s)	3.165	2.141	Hydroxyapatite	4.066	2.49
Anhydrite	–1.814	–1.823	Lepidocrocite	8.586	9.271
Aragonite	–0.564	–0.329	Mackinawite	–1.163	–0.363
Brucite	–3.561	–2.42	Magnesite	0.889	1.232
$Ca_3(PO_4)_2$ (beta)	–1.598	–2.972	Magnetite	24.919	27.777
$CaCO_3xH_2O$(s)	–1.747	–1.498	$MnCO_3$ (am)	–0.882	–0.041
Calcite	–0.408	–0.17	$MnHPO_4$(s)	1.006	0.113
Chalcedony	0.21	0.201	Na-Jarosite	2.433	1.814
Cristobalite	0.013	0.005	Pyrite	6.746	12.621
Diaspore	4.792	4.356	Quartz	0.686	0.685
Dolomite (disordered)	0.503	0.908	Rhodochrosite	–0.4	0.435
$Fe(OH)_2$ (c)	–2.44	–0.354	Sepiolite (A)	–0.069	2.672
$Fe_3(OH)_8$(s)	10.14	13.596	Siderite	–0.455	0.428
Ferrihydrite	5.772	6.169	SiO_2 (am)	–0.645	–0.667
FeS (ppt)	–1.921	–1.152	Spinel	–0.642	–0.568
Gibbsite (C)	3.905	3.464	Strengite	1.828	–0.429
Goethite	8.873	9.383	Struvite	–2.818	–3.508
Gypsum	–1.486	–1.471	Variscite	0.216	–2.867
Hematite	20.069	21.068	Vaterite	–1.019	–0.793
H-Jarosite	–4.352	–5.783	Vivianite	0.282	0.727

* Calculated by using PHREEQC Version 3 code with the following input values (S_1/S_2): temperature = 9.2/4.8°C, pH = 7.7/8.2, ionic strength = 0.06/0.04 M, O_2 = 0.002/0.06 mM, Alkalinity (as HCO_3^-) = 177/147 mg L^{-1}, DOC = 12 mg L^{-1}, DIC = 9.0 mM, Na^+ = 24.0/17.0 mM, K^+ = 0.31/0.27 mM, Ca^{2+} = 4.0/3.7 mM, Mg^{2+} = 445.0 mM, Si = 0.29/0.25 mM, Al^{3+} = 0.05 mM, Fe^{2+} = 0.028/0.117 mM, Fe^{3+} = 0.172/0.131 mM, Mn^{2+} = 0.01/0.04 mM, PO_4^{3-} = 0.02/0.001 mM, SO_4^{2-} = 16.0/20.0 mM, HS^- = 0.00025 mM, NO_3^- = 0.017/0.040 mM, and NH_4^+ = 0.127/0.142 mM for –190 mV and –80 mV, respectively.

reductive dissolution, releasing Ce^{3+}, which becomes incorporated into carbonates. As carbonate recrystallization and dissolution cycles proceed, the carbonate fraction acquires positive Ce anomalies (Fig. 5C; Table 2). Our data highlight that sedimentary carbonates exhibit relative stability against REE redistribution under Eh fluctuations compared to other phases. However, when considered alongside the complexity of LM sedimentary textures and composition (Fig. 5D, E), particularly the coexistence of composite aggregates with detrital and/or authigenic grains, our data reveal a heterogeneity often overlooked in bulk-sediment analyses. Those analyses tend to oversimplify mineralogical variability and elemental partitioning.

LM Carbonate and Sulfur Budgets as Inferred Using $\delta^{13}C$ and $\delta^{34}S$ Analysis

$\delta^{13}C$ of Dissolved Inorganic Carbon.—Gradients of pH and DIC in the LM water column can be influenced by the complex interplay between microbial activity, mineral dissolution/precipitation reactions, and their redox sensitivity (Soetaert et al. 2007; Middelburg 2019). As pH decreases with increasing water depth (Fig. 3B), DIC concentrations increase substantially from 1.9 to 9.8 mM (Fig. 6A; Table 1). Alongside this increase, DIC $\delta^{13}C$ values also decrease downwards from 0.1 to –3.9‰, signaling a ^{13}C-depleted hydrochemical input from the lakebed. Potential sources of this ^{13}C depletion include: i) geogenic CO_2 influx with $\delta^{13}C$ values that lean towards –4.0‰ (Weinlich et al. 1999; Krauze et al. 2017), and/or ii) respiration of sedimentary organic matter, which in LM exhibits a narrow $\delta^{13}C$ range of –27.9 ± 0.1‰ (N = 6).

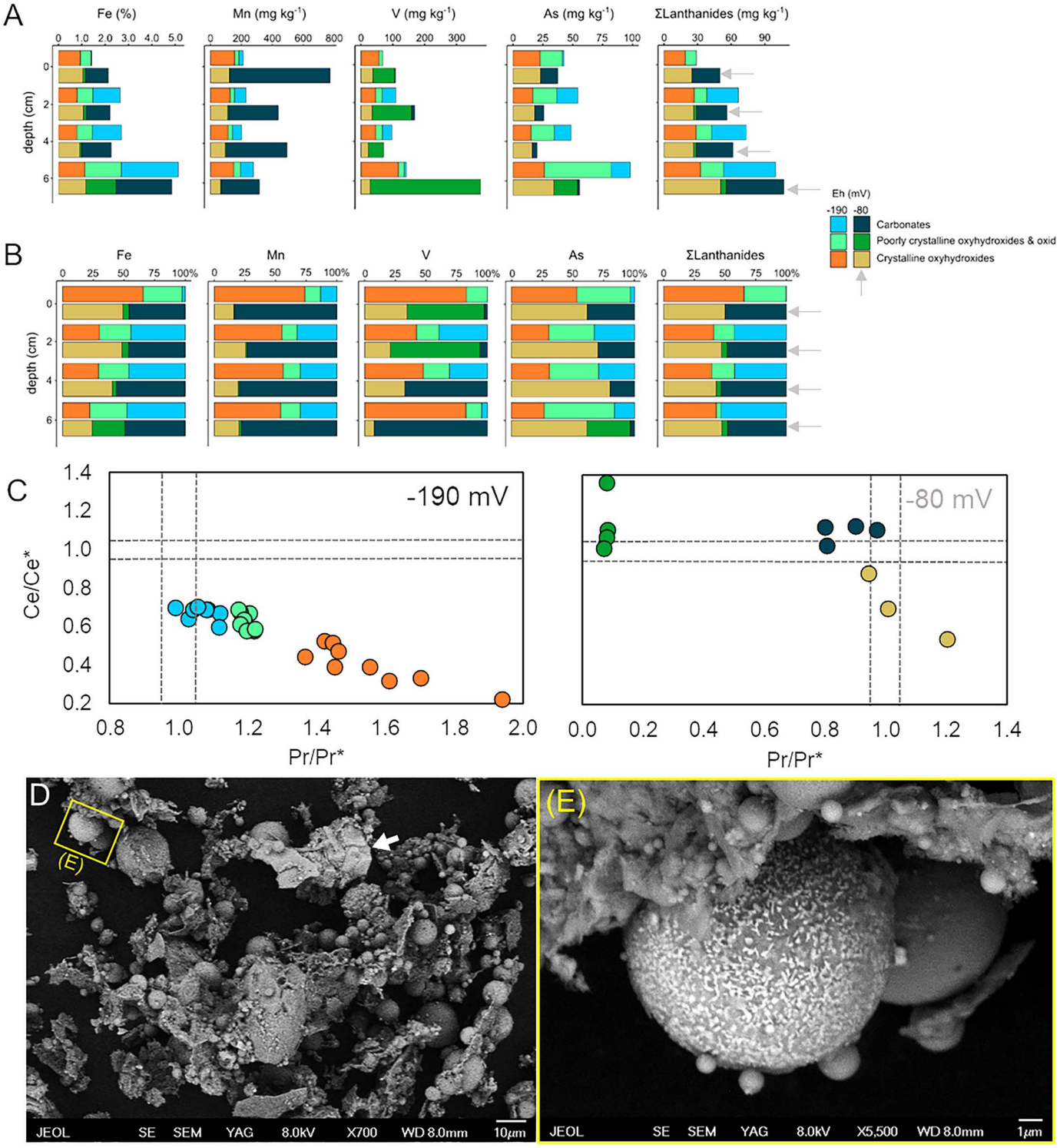

FIG. 5.—Elemental concentrations and metal-partitioning dynamics. **A)** Mineral-specific concentrations of Fe, Mn, Σlanthanides, V, and As in Lake Medard (LM) sediments at three depth intervals (0–2 cm, 2–4 cm, 4–6 cm), determined by sequential extraction. Each stacked bar shows the fraction bound to carbonates, poorly crystalline oxyhydroxides, or crystalline oxyhydroxides. Gray arrows denote samples from an overlying water-column Eh of –80 mV, facilitating direct comparison to the more common –190 mV condition. **B)** Normalized distribution of analytes in Fe_{HR} phases (combining carbonate-bound, poorly crystalline oxyhydroxides, and crystalline oxyhydroxides) expressed as a percentage of total detected concentrations, underscoring changes in metal partitioning. **C)** Plot of Ce anomaly (Ce/Ce*) versus Pr anomaly (Pr/Pr*), illustrating redox-driven Ce^{3+} solubilization and subsequent incorporation into carbonates under transient reducing conditions. **D)** Scanning electron micrograph of upper-sediment aggregates showing complex multiphase particles, including detrital siderite grains (white arrow). The yellow box encloses the region magnified in Part E. **E)** Higher-magnification SEM image highlighting a spherical Fe-bearing aggregate, with visible surface texture features indicative of mineral accretion processes.

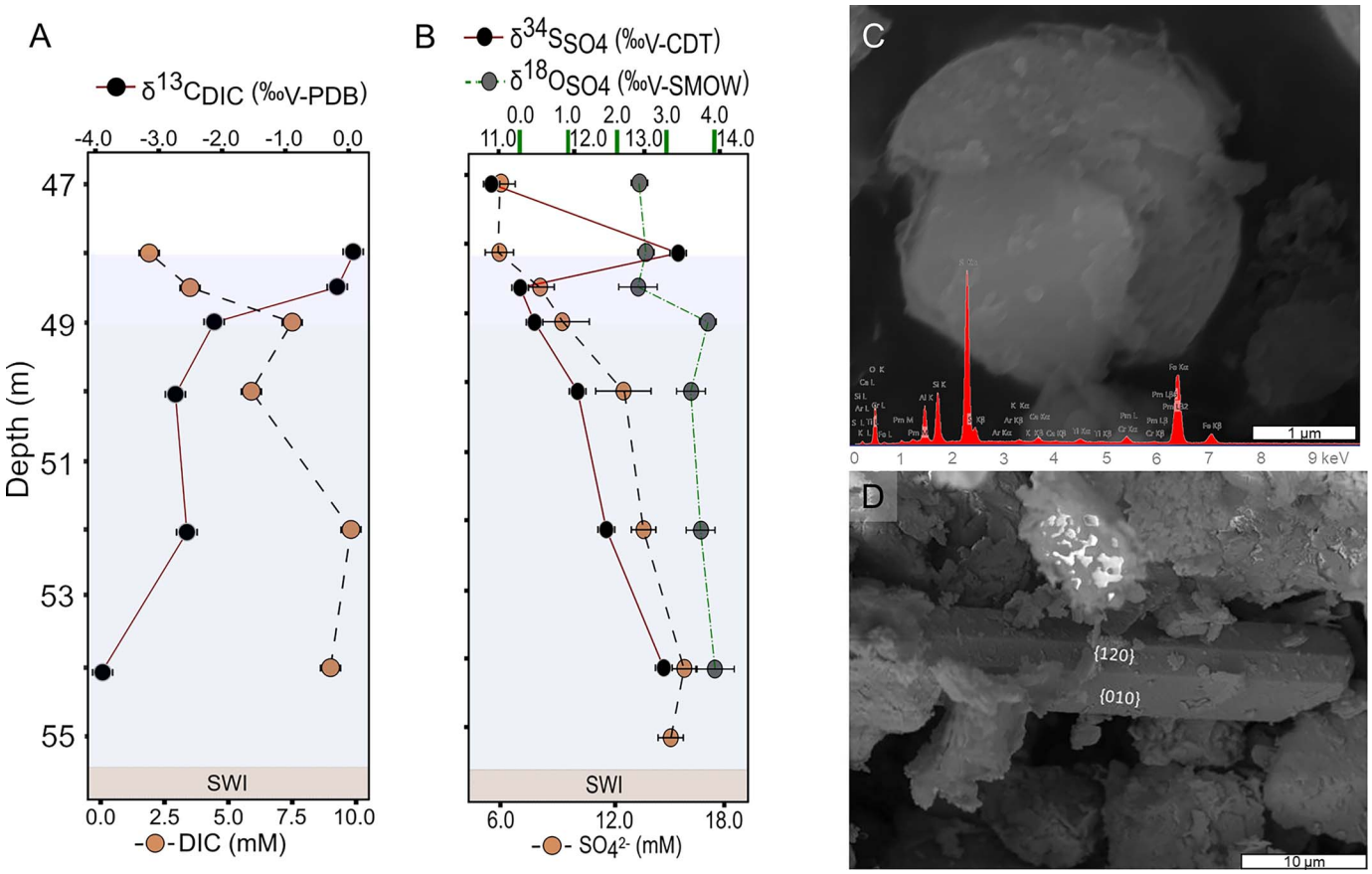

FIG. 6.—Hydrochemical isotope data in LM. **A)** Downward increase in DIC concentrations from 1.9 to 9.8 mM, accompanied by a decrease in DIC-$\delta^{13}C$ values from 0.1 to –3.9‰, likely indicating a ^{13}C-depleted hydrochemical DIC input from the lakebed. **B)** $\delta^{34}S$ and $\delta^{18}O$ values of dissolved sulfate (dSO_4^{2-}) showing a positive correlation with residual sulfate concentrations and a decoupled +2.2‰ increase in dSO_4^{2-}–$\delta^{34}S$ values at the chemocline, suggesting sulfur isotope evolution due to abiotic oxidation (see text for details). **C)** Octahedral pyrite is dispersed in the sediments and exhibits $\delta^{34}S$ values in the range –35.1 to –23.0‰. **D)** Euant gypsum microcrystals form by reaction of pore water sulfate evolved after disproportionation of intermediate sulfur species with Ca^{2+}, resulting in ^{34}S-depleted ($\delta^{34}S$ = –13.9‰ to –9.6‰), ^{18}O-enriched ($\delta^{18}O$ +5.1‰ to +6.3‰) sulfate-gypsum.

$\delta^{34}S$ and $\delta^{18}O$ Values of Dissolved SO_4^{2-}.—Ranging from +10.9 to +13.4‰ (Fig. 5B), the $\delta^{34}S$ values of dSO_4^{2-} shows a statistically significant positive correlation with the dSO_4^{2-} concentrations (Pearson coefficient ≈ 0.970, p-value < 0.01; Table 1). The $\delta^{18}O$ values of SO_4^{2-} range from +2.0‰ to +4.0‰. The S and O isotope signals appear to be decoupled at the chemocline, where $\delta^{34}S$ of residual sulfate shows a + 2.2‰ shift not affecting its $\delta^{18}O$ (Fig. 5B). This points to S isotopes in dSO_4^{2-} evolving faster at this level than the corresponding O isotope ratio. Sulfur cycling near the chemocline in the presence of trace amounts of Fe^{2+} and under dysoxic conditions, or autoxidation, can drive the production of isotopically enriched S without causing O-isotope fractionation in the residual dSO_4^{2-} (Canfield 2001; Fritz and Fontes 1986; Turchyn and Schrag 2006; Eldridge and Farquhar 2018).

Analyses of Sedimentary $\delta^{13}C$ and $\delta^{34}S$

Siderite.—Miocene siderite in carbonate-rich layers in the Cypris Formation exhibits $\delta^{13}C$ values between +8.5 to +10.6‰ (N = 6). The bulk $\delta^{13}C$ values of LM sediments, on the other hand, are +6.4 ± 0.3‰ (N = 6), and can be principally attributed to siderite as per our semiquantitative XRD data summarized in Figure 4A. Exhibiting a $\delta^{13}C$ offset of 9.1‰ to 10.9‰ compared to bottom-water DIC (mean $\delta^{13}C$ value –3.9‰), the bulk sediment $\delta^{13}C$ values are seen as a signature conferred by detrital carbonates sourced from Miocene strata in the former lignite mine overburden. These minerals now constitute the modern lakebed, and would have been introduced to the mine spoils or during the infilling stage of the lake system, when erosion of the overburden occurred. A small proportion of siderite (or any other carbonate phase at an abundance ≤ 0.5 wt.%; i.e., not detected by XRD), however, might have formed on the lakebed, influencing the bulk-sediment $\delta^{13}C$ signature towards less positive values compared to Miocene carbonates. Yet, the $\delta^{13}C$ offset indicates that most carbonates in present-day LM sediments are non-authigenic but detrital.

Gypsum.—The isotope compositions of gypsum ($\delta^{34}S_{gy}$) and pyrite ($\delta^{34}S_{py}$) constituting the sediments are shown in Figure 5C and D. The $\delta^{34}S_{gy}$ values range from –13.9‰ to –9.6‰, showing ^{34}depletion of –17.8‰ to –11.6‰ relative to the values measured in dissolved SO_4^{2-}. The $\delta^{18}O_{gy}$ values range from +5.1‰ to +6.3‰, indicating that the sulfate in gypsum is enriched in ^{18}O by up to +2.6‰ compared to the $\delta^{18}O$ in the dissolved phase. These values also differ substantially from possible detrital phases (Fig. S2; Šmejkal 1979).

Pyrite.—In LM sediments the $\delta^{34}S_{py}$ values range from –35.1 to –23.0‰. The Miocene overburden has pyrite with $\delta^{34}S_{py}$ values between +8 and +27‰ (median 16‰) (Fig. S2), which indicates that pyrite is not a detrital (redeposited) phase, but an authigenic one—it records fractionation of around 38‰ to 28‰ relative to the $\delta^{34}S_{SO4}$ values measured in

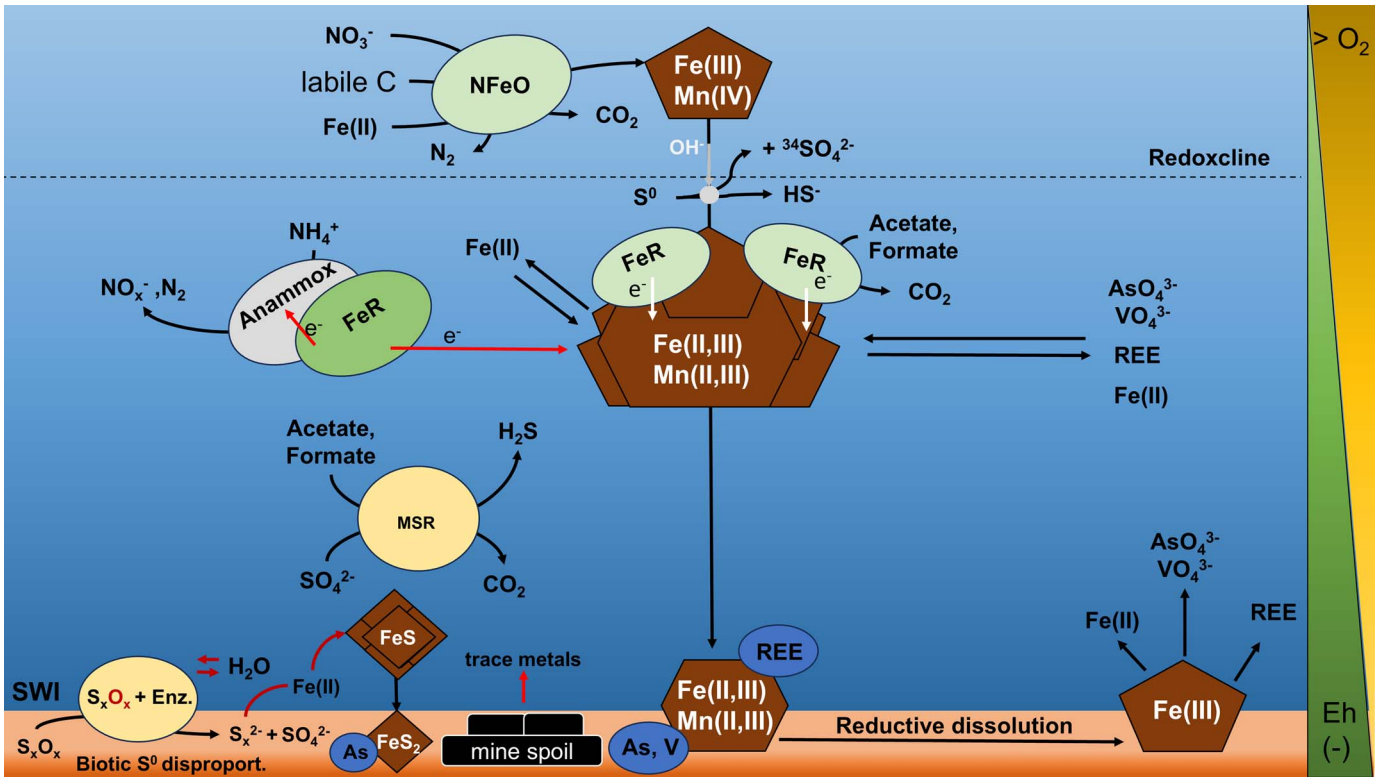

FIG. 7.—Schematic representation of biogeochemical processes at the SWI illustrates the redox gradients and associated transformations. The scheme includes key elements and compounds such as O_2, NO_3^- and NH_4^+, Fe, Mn, REE, arsenate (AsO_4^{3-}), vanadate VO_4^{3-}), and various sulfur species (SO_4^{2-}, SO_3^{2-}, H_2S). Processes such as reductive dissolution, iron and manganese reduction, and MSR, and enzymatic disproportionation of intermediate sulfur are depicted, along with the influence of labile carbon and electron transfer (e^-). The chemocline and associated Eh range are indicated, highlighting the complex interplay between geochemical and microbial activities in these compartments of LM's water column. The potential for sulfide autoxidation and mixed source sulfate is also noted, as well as the accessory formation of pyrite with $\delta^{34}S$ fingerprints consistent with the disproportionation of intermediate sulfur species, as documented by Petrash et al. (2022).

monimolimnial waters, consistent with variable fractionations associated with MSR (e.g., Brüchert 2004).

DISCUSSION

Redox Stratification and Seasonal Variability

Lake Medard is characterized by a strongly stratified ferruginous, manganous, and nitrogenous hypolimnion, with substantial dSO_4^{2-} (Fig. 3C, D; Table 1), which is unusual in stable ferruginous lakes. Seasonal variations in groundwater recharge and precipitation strongly influence the depth of the chemocline, thereby modulating Eh, conductivity gradients, and elemental fluxes (Petrash et al. 2022). The role of groundwater recharge is important in controlling dSO_4^{2-} dynamics. Decreased groundwater influx reduces the dissolution of sulfate-bearing salts present in the underlying bedrock, which contains fractures associated with epithermal mineralization (Pačes and Šmejkal 2004). This results in lower bottom-water density and deeper chemocline positioning (Boehrer and Schultze 2008). Consequently, LM exhibits lateral variability in sulfate concentrations due to differences in water-column stratification.

Our monitoring campaigns revealed an inverted thermocline in winter, with temperature increasing at depth due to surface cooling and the presence of denser bottom waters. These temperature-driven density differences shape redox structure and influence Fe cycling. The dynamic nature of the bottom LM water column, particularly the fluctuating hypolimnion redox gradients, underscores the need for multi-seasonal monitoring to fully capture these biogeochemical interactions.

Microbial Controls on Cycling of Iron, Nitrogen, Manganese, and Sulfur

Reactive Particles and Iron Snow.—Iron-bearing colloids and aggregates (i.e., iron snow) play a pivotal role in metal sequestration and Fe cycling (Reiche et al. 2011). In LM, these sinking reactive particles are formed at the chemocline, where microbial Fe(II) oxidation (exerted by, e.g., species belonging to the family Gallionellaceae) produces amorphous Fe(III)-oxyhydroxides that scavenge trace elements such as lanthanides, V, and As (Anderson and Pedersen 2003) (Fig. 7). As these particles descend, Fe(III)-reducing bacteria (e.g., *Geobacter* spp.) initiate recrystallization, leading to the formation of poorly crystalline oxyhydroxides, such as lepidocrocite, which can eventually transform into goethite (Posth et al. 2014; Schulzet al. 2023). The interactions between Fe(II)-oxidizers and Fe(III)-reducers modulate Fe cycling, affecting reactive mineral stability and metal solubility and retention in LM sediments, while lepidocrocite and goethite transformations can modulate the availability of Mn in solution (Davies and Morgan 1989).

Coupled Nitrogen-Iron Transformations.—Oxidation of ferrous iron oxidation coupled to nitrate utilization (NDFeO) and anaerobic ammonium oxidation (anammox) can co-occur near the chemocline, contributing to N losses not fully captured by NH_4^+ and NO_3^- profiles (Fig. 3; Wang et al. 2022). Below this zone, dFe^{2+} concentrations rise as NDFeO diminishes, giving MSR a more prominent role (Fig. 7). While detailed NO_2^- profiles could not be fully resolved due to high chloride interference, the redox-sensitive Fe-N interactions suggest overlapping N and Fe cycling mechanisms, particularly in chemocline transition, where anammox-favorable conditions may

exist (Fig. 7). Evidence for these processes and their interaction with sulfatic waters in LM, as in marine systems (Lyons et al. 2024), thus remain limited due to sampling and analytical challenges.

Sulfate Reduction and Pyrite Formation.—In the studied water column and SWI, SRB use dSO_4^{2-} (up to ~ 17.5 mM) to generate H_2S, which readily reacts with Fe(III)-oxyhydroxides to form pyrite precursors (Berner 1984). Sulfate reduction near the SWI contributes to elemental cycling, as suggested by a minor yet measurable decline in dSO_4^{2-} concentrations (0.8 mM) at the SWI. However, limited labile organics (volatile fatty acids ≤ 80 nM) and H_2S reoxidation by iron snow constrain significant precursor pyrite formation and subsequent pyrite accumulation (Fig. 7). Members of the family Desulfobulbaceae, present in the monimolimnion microbial community assemblage (Petrash et al. 2022), may engage in electron transfer via conductive minerals in iron-snow aggregates, influencing Fe-S cycling and trace-metal sequestration (Valero et al. 2024). The limited accumulation of pyrite in LM suggests that H_2S oxidation by Fe(III) oxyhydroxides constrains long-term sulfur sequestration (see Berner 1984).

The $\delta^{34}S$ data suggest that a proportion of H_2S is reoxidized before incorporation into pyrite, causing sulfur isotope fractionation consistent with an open-system oxidative S cycling (Canfield 2001). It is noteworthy that the $\delta^{34}S_{gy}$ values are relatively closer to $\delta^{34}S_{py}$ than to $\delta^{34}S$ in the dSO_4^{2-}, possibly implying a common S source, such as H_2S and SO_4^{2-} derived from the disproportionation of intermediate S species (generally referred to as S^0; Fig. 7). An evaluation of the $\delta^{18}O$ in the dissolved and solid SO_4^{2}-bering phases corroborates this interpretation (Petrash et al. 2022). Intracellular biogeochemical reactions in which bacteria gain energy from disproportionation cause the residual sulfate-O to become isotopically heavier (Böttcher et al. 2001; Turchyn and Schrag 2006). In consequence, gypsum that precipitates at or near the SWI is enriched in ^{18}O. It is noteworthy that the isotopic composition of gypsum in LM differs considerably from sulfate minerals in the mine spoils and in the overburden (Fig SM2).

Trace-Element Partitioning: REE, V, and As

REE Cycling and Ce Anomalies.—Redox gradients in LM strongly influence the partitioning of REE among oxyhydroxides, carbonates, and residual aqueous phases (Burdige 1993; Tostevin 2021; Hatje et al. 2024). REE behavior in the water column of LM is also controlled by Fe(III)-oxyhydroxide transformations and microbial interactions occurring at the interface between water and particulate matter (Valdés et al. 2024; Fig. 7).

Element concentrations in LM sediments show relative enrichment when normalized against standard geochemical baselines or against concentrations measured in local sedimentary sources to the modern lake system (Fig. SM3). In the upper sediments, LREE preferentially sorb onto amorphous and poorly crystalline Fe(III)-oxyhydroxides in settling iron snow, while HREE remain more mobile and recomplex near or at the chemocline. Vertical variations in Ce^{3+}/Ce^{4+} highlight the complexity of using Ce anomalies as stand-alone redox proxies (Zhang and Shields 2022).

We interpret that variability in carbonate REE datasets results from dissolution–precipitation reactions involving coexisting easy reducible (metastable) phases with marked REE affinity and reactivity at the SWI (Fig. 7). Carbonate phases can incorporate Ce released from easily reducible oxyhydroxides; their resulting moveable signal therefore reflects short-lived diagenetic conditions rather than long-term diagenetic processes. Rapid sedimentation can preserve that moveable signal, but oxygenation and deoxygenation stages (e.g., seasonal development of hypoxia) may lead to high variability and even a reset of primary ambient conditions in any given ancient sedimentary record.

The availability of aqueous Mn and the complexation dynamics of REE with Mn(IV)-oxyhydroxides are highly sensitive to Eh transitions in the chemocline (Fig. 7). Therefore, the redox behavior of Mn in the water column may play a prominent role in the transfer of REE (and other trace metals) to the SWI. Those dynamics can also affect their subsequent uptake by relatively less redox-sensitive authigenic phases, such as carbonates and crystalline oxyhydroxides (Tostevin 2021). Fe(III)- and Mn(IV)-oxyhydroxides and carbonates are corroborated as the main phases governing siderophile metal cycling in sedimentary environments. Phyllosilicates, by contrast, are usually considered poorly reactive or unreactive with regard to sulfide over short timescales (Raiswell and Canfield 1996), and at the physicochemical conditions encountered in LM. However, electron transfer between Fe(III) and inner sphere-complexed sulfide may occur during burial (Poulton et al. 2004). Therefore, a note of caution on this generalized assumption is provided below.

Dynamics of Vanadium and Arsenic.—Vanadium exhibits a strong affinity for poorly crystalline Fe(III)-oxyhydroxides under higher Eh, shifting to carbonate complexes or crystalline phases under more reducing conditions (Fig. 5; Posth et al. 2014). Arsenic tends to associate with carbonates when a more marked redox gradient exists at the chemocline (S_1), but shifts toward being preferentially bound to Fe(III)-oxyhydroxides when the redox potential increases (S_2). This behavior suggests variable interactions with crystalline Fe(III) phases that comprise sediments initially deposited on the abandoned mine floor. Notably, the lower strata of LM sediments were once rich in jarosite (e.g., Murad and Rojiík 2003), which exhibits high affinity for As (Karimian et al. 2017). Over time, however, this altered jarosite transitioned to goethite, which now dominates the iron-bearing mineralogy of the lakebed, together with minor siderite and accessory pyrite. Fluctuations in redox potential also enable microbial As(V) reduction and As(III) oxidation/detoxification, particularly coupled with Fe and S cycling (Saunders et al. 2019; Oremland and Stolz 2003), and could be governed by mineral–microbe electron-transfer mechanisms. These mechanisms appear to further enhance As sequestration in authigenic phases formed and exported from the dynamic redox interface in LM (Valero et al. 2023).

A Note of Caution: The Role of Phyllosilicates in Elemental Cycling

While Fe(III)- and Mn(IV)-oxyhydroxides and carbonates are widely recognized as the dominant phases governing Fe (and siderophile metal) cycling in sedimentary environments (Poulton and Raiswell 2002; Raiswell and Canfield 2012), the role of phyllosilicates in elemental mobility should not be overlooked. Phyllosilicates are generally considered geochemically inert over short timescales pertaining to the LM system, leading to the assumption that they would play a rather minimal role in the trace-metal dynamics. However, recent studies highlight interactions with clay minerals that we may have overlooked and can significantly impact element solubility (see Li et al. 2024 for a review). In addition, it has been long known that structural Fe(III) in clay minerals can undergo microbial reduction (Kostka et al. 1999; Stucki and Kostka 2006). Over longer diagenetic timescales, transformations involving kaolinite and Fe(III)-oxyhydroxides can lead to the formation of Fe(II)-smectite and, eventually, Fe(II)-rich illite, which influences the ability of this sediment fraction to participate in metal retention and redistribution (Lanson et al. 2002; Stucki 2011). Although these processes were not explicitly quantified in this study, their potential influence on elemental cycling in modern systems undergoing stabilization, as well as ancient early diagenetic environments, remain an open question. Given LM's possible use as a natural laboratory for studying trace-metal dynamics, future research should consider the interplay between the kinetics of clay-mineral transformations and geochemical proxies to refine interpretations of element mobility in both modern and ancient systems.

DIC Sources and Carbonate Stability

Gradients of pH and DIC reflect both geogenic CO_2 inputs ($\delta^{13}C \approx -1.9$ to -4.0 ‰) from regional Eger Rift faults (Weinlich et al. 1999; Mach et al. 2017; Liu et al. 2020) and in-lake microbial respiration of organic matter (see Middelburg 2019). Carbonate minerals in LM's sediments match

Miocene overburden facies (Murad and Rojík 2003; Kříbek et al. 2017), suggesting a detrital origin. The ~ 10‰ offset between bulk sediment $\delta^{13}C$ and bottom-water DIC underscores this predominantly allochthonous source (Krauze et al. 2017). Future work quantifying respiration-driven $\delta^{13}C$ shifts would refine interpretations of carbon cycling in this oligotrophic setting (Havas et al. 2023a, 2023b).

Pyritization Potential

Although LM is anoxic and ferruginous near the SWI ($Fe_{HR}/Fe_T > 0.7$), limited labile organic compounds, along with ongoing H_2S oxidation by Fe(III)- and Mn(IV)-oxyhydroxides, restrict large-scale pyrite formation ($Fe_{py}/Fe_{HR} \leq 0.25$). In this context, quantitative MSR can be outpaced by the rapid reaction of H_2S with FeOOH phases, which are formed continuously through the transformation of metastable Fe(II) oxidation products (potentially including ferrihydrite). This reaction prevents significant accumulation of H_2S in the sediment and LM's density-stratified waters (Petrash et al. 2022). Consequently, only small, dispersed amounts of pyrite, exhibiting pentagonal or octahedral habits, accumulate. A shift toward higher trophic states could favor more extensive pyritization (Raiswell et al. 2018). A more detailed monitoring of the sedimentary and isotopic response to these Eh oscillations can provide a valuable modern analog for deciphering further details of the early diagenetic reactions possibly involving microbial iron and/or sulfur respiration, offering insights into how short-term environmental changes are recorded in the sedimentary record.

CONCLUSIONS

This study highlights the interplay between redox stratification, microbes, and mineral interactions in the water column and sediments of LM. Seasonal variability in the depth of the chemocline creates a dynamic early diagenetic setting in which ferruginous and manganous conditions can transition to more oxidizing, sulfate-influenced regimes under oligotrophic states, transition toward pyrite formation under mesotrophic states, or even evolve into sulfidic conditions at higher trophic levels.

Underlying these changes, Fe- and N-based metabolisms dominate a series of interlinked biogeochemical cycles impacted by minor suboxic to anoxic range fluctuation in Eh (Eh ≤ 30 mV) that strongly regulate trace-element partitioning (particularly REEs, As, and V) and stable-isotope signals of the sedimentary system. The metabolic pathways involved are largely cryptic—functionally significant but difficult to observe due to low reaction rates, overlapping geochemical signals, or masking by dominant biogeochemical processes. In this redox-dynamic setting, carbonate phases largely preserve their primary REE signatures, though they may incorporate REE from pore waters during episodes of water-column redox fluctuations. This complexity is further reflected in the post-mining lake sedimentary record, where poorly crystalline oxyhydroxides, carbonates, and minor pyrite variably participate in element retention or solubilization under fluctuating redox states. At the same time, isotopically distinct sulfur phases—sulfate and sulfide—highlight open-system S cycling that is only partially expressed in the aqueous environment.

The data presented here collectively show that LM redox structure promotes significant Fe enrichment in the sediments ($Fe_{HR}/Fe_T \geq 0.7$), yet only a modest degree of pyritization, owing to the limited accumulation of dH_2S. As the latter remains low in the system, Fe delivered to the sediment via Fe(III)-oxyhydroxides continuously act as a redox buffer, aided by the presence of siderite, which in turn buffers the system pH. These findings highlight the transitory nature of redox boundaries in recently formed modern lacustrine systems, or any ancient system resembling LM. More broadly, they emphasize the caution required when drawing parallels to ancient analogs, where diagenetic overprints and incomplete capture of ephemeral redox fluctuations can complicate paleoredox reconstructions.

Future Research Directions

Looking ahead, several topics remain unanswered that could shape further investigations:

Resolving Intermediate Nitrogen Species and Iron-Anammox Linkages.—Higher-resolution measurements of intermediate nitrogen species (e.g., NO_2^-) and stable-isotope analyses of nitrogen ($\delta^{15}N$) and oxygen bound to nitrogen ($\delta^{18}O$) across the LM chemocline could clarify the relative roles of nitrate-dependent Fe(II) oxidation versus anammox-mediated nitrogen removal. Precision sampling using a remotely operated vehicle (ROV) equipped with syringe-based collectors would minimize disturbance during water-column profiling. Alternatively, and more realistically, as per funding limitations, combining *in situ* sampling (e.g., via specialized Niskin bottles with fixatives) with immediate subsampling in an on-board glove box purged with inert gas, or indirectly using ^{15}N tracer incubations, could provide higher-resolution depth profiles and quantify N reaction rates under transiently augmented redox states. Such data would help resolve the partitioning of NO_3^- between Fe(II) oxidation and anammox pathways, offering deeper insights into how N loss is modulated by Fe cycling under variable redox regimes developed in the water column.

Quantifying Microbe–Mineral Interactions.—Targeted microbial surveys, in tandem with experiments based on redox-sensitive tracers (e.g., stable Fe, N, and/or S isotopes), would further clarify the specific metabolic pathways active at the chemocline and in sinking particulate matter. These approaches may highlight the extent to which electron shuttling and microbially mediated mineral dissolution drive metal mobility. Meanwhile, molecular (metagenomic and metatranscriptomic) profiling, though not a direct measurement of chemical species, can identify active N-transforming microbes and their functional genes—indicating where and when intermediate species are likely to temporarily accumulate. This would also reveal the suite of microbially controlled N-based reactions involving reactive iron transformations that such temporary accumulations can influence.

Refining the Role of Manganese and Trace-Metal Cycling.—Given the sensitivity of Mn redox state to minor Eh shifts, a closer examination of Mn(II) oxidation kinetics and subsequent Mn(III)-oxyhydroxide formation could reveal additional pathways for REE partitioning and carbonate cementation under fluctuating redox conditions.

Assessing the Fate of Organotrophic Respiration and Geogenic CO_2.—Detailed isotope mass-balance approaches would help distinguish between carbon from microbial mineralization of organic matter versus carbon from deep-seated CO_2, clarifying its role in driving pH and DIC shifts in the hypolimnion.

Evaluating Parasequence-Scale Diagenetic Implications.—Studies linking short-term redox cycles in LM to longer-term diagenetic transformations (e.g., Fe-smectite (trans)formation, Ca-sulfate precipitation, or changes in pyritization extent) could improve our understanding of how ephemeral water-column processes become preserved—or overprinted—in the sedimentary record. In this regard, laboratory-simulated diagenesis based on sediment incubations conducted under environmentally relevant O_2 limitations can produce valuable insight.

By pursuing these research directions, it would be possible to better resolve the delicate balance of biogeochemical reactions that govern not only LM present-day hydrochemistry but also help refine our interpretations of ancient redox-stratified environments. Ultimately, bridging modern biogeochemical processes with the rock record strengthens paleoenvironmental reconstructions, offering a clearer view of how microbe–mineral interactions have shaped Earth's evolving (sub)surface environments.

ACKNOWLEDGMENTS

The authors have no conflicts of interest to declare. The constructive guidance of Camille Thomas and an anonymous reviewer at JSR, along with the editorial inputs of Branimir Šegvić, Stephen E. Kaczmarek, and John B. Sutherland, are sincerely appreciated. They substantially improved this manuscript. Our sincere thanks go to Jiři Jan and Jakub Borovec for assistance during limnological sampling campaigns, and Stefan Lalonde (Université de Bretagne Occidentale) for conducting water column element concentration determinations. We thank Daniel Grolimund and Dario Ferreira Sanchez at the Paul Scherrer Institute for instrumental support and expert advice during beamline experiments at MicroXAS (under SLS-PSI 20161155). This study was made possible by financial support from the Research Organization Long-term Development Concept of the Czech Geological Survey for the period 2023–2027 (636100), which supported manuscript preparation, and from Czech Science Foundation (GACR; Grant No. 19-15096Y) which funded sampling and data gathering.

OPEN RESEARCH

All data supporting the findings of this study are available in Tables 1–3 of this article and in Supplemental Material.

REFERENCES

Algeo, T.J., and Liu, J., 2020, A re-assessment of elemental proxies for paleoredox analysis: Chemical Geology, v. 540, p. 119549.

Anderson, C.R., and Pedersen, K., 2003, In situ growth of *Gallionella* biofilms and partitioning of lanthanides and actinides between biological material and ferric oxyhydroxides: Geobiology, v. 1, p. 169–178.

Berner, R.A., 1984, Sedimentary pyrite formation: an update: Geochimica et Cosmochimica Acta, v. 48, p. 605–615.

Boehrer, B., and Schultze, M., 2008, Stratification of lakes: Reviews of Geophysics, v. 46, no. 2006RG000210.

Böttcher, M.E., Thamdrup, B., and Vennemann, T.W., 2001, Oxygen and sulfur isotope fractionation during anaerobic bacterial disproportionation of elemental sulfur: Geochimica et Cosmochimica Acta, v. 65, p. 1601–1609.

Bouška, V., and Pešek, J., 1999, Quality parameters of lignite of the North Bohemian Basin in the Czech Republic in comparison with the world average lignite: International Journal of Coal Geology, v. 40, p. 211–235.

Brüchert, V., 2004, Physiological and ecological aspects of sulfur isotope fractionation during bacterial sulfate reduction, *in* Amend, J.P., Edwards, K.J., and Lyons, T.W., eds., Sulfur Biogeochemistry: Past and Present: Geological Society of America, Special Paper 379, p. 1–16.

Burdige, D.J., 1993, The biogeochemistry of manganese and iron reduction in marine sediments: Earth-Science Reviews, v. 35, p. 249–284.

Canfield, D.E., 2001, Biogeochemistry of sulfur isotopes: Reviews in Mineralogy and Geochemistry, v. 43, p. 606–636.

Clarkson, M.O., Poulton, S.W., Guilbaud, R., and Wood, R.A., 2014, Assessing the utility of Fe/Al and Fe-speciation to record water column redox conditions in carbonate-rich sediments: Chemical Geology, v . 382, p. 111–122.

Davies, S.H.R., and Morgan, J.J., 1989, Manganese(II) oxidation kinetics on metal oxide surfaces: Journal of Colloid and Interface Science, v. 129, p. 63–77.

Davis, A., Lengke, M., Sims, N., and Roth, M., 2024, A review of viable mineral precipitates in pit lake modeling: Mine Water and the Environment, v. 43, p. 340–367.

Davison, W., 1993, Iron and manganese in lakes: Earth-Science Reviews, v. 34, p. 119–163.

Eldridge, D.L., and Farquhar, J., 2018, Rates and multiple sulfur isotope fractionations associated with the oxidation of sulfide by oxygen in aqueous solution: Geochimica et Cosmochimica Acta, v. 237, p. 240–260.

Evans, C.H., 2013, Biochemistry of the Lanthanides: New York, Springer, 444 p.

Fritz, P., and Fontes, J.C., eds., 1986, Handbook of Environmental Isotope Geochemistry: The Terrestrial Environment: Berlin, Springer, 951 p.

Hatje, V., Schijf, J., Johannesson, K.H., Andrade, R., Caetano, M., Brito, P., Haley, B.A., Lagarde, M., and Jeandel, C., 2024, The global biogeochemical cycle of the rare earth elements: Global Biogeochemical Cycles, v. 38, p. 14–53.

Havas, R., Thomazo, C., Iniesto, M., Jézéquel, D., Moreira, D., Tavera, R., Caumartin, J., Muller, E., López-García, P., and Benzerara, K., 2023a, Biogeochemical processes captured by carbon isotopes in redox-stratified water columns: a comparative study of four modern stratified lakes along an alkalinity gradient: Biogeosciences, v. 20, p. 2347–2367.

Havas, R., Thomazo, C., Iniesto, M., Jézéquel, D., Moreira, D., Tavera, R., Caumartin, J., Muller, E., López-García, P., and Benzerara, K., 2023b, The hidden role of dissolved organic carbon in the biogeochemical cycle of carbon in modern redox-stratified lakes: Biogeosciences, v. 20, p. 2405–2424.

Havas, R., Thomazo, C., Caumartin, J., Iniesto, M., Bert, H., Jézéquel, D., Moreira, D., Tavera, R., Bettencourt, V., López-García, P., and Vennin, E., 2025, Untangling the primary biotic and abiotic controls on oxygen, inorganic and organic carbon isotope signals in modern microbialites: Geobiology, v. 23, no. e70012.

Karimian, N., Johnston, S.G., and Burton, E.D., 2017, Antimony and arsenic behavior during Fe(II)-induced transformation of jarosite: Environmental Science and Technology, v. 51, p. 4259–4268.

Kostka, J.E., Haefele, E., Viehweger, R., and Stucki, J.W., 1999, Respiration and dissolution of iron (III)-containing clay minerals by bacteria: Environmental Science & Technology, v. 33, p. 3127–3133.

Krauze, P., Kämpf, H., Horn, F., Liu, Q., Voropaev, A., Wagner, D., and Alawi, M., 2017, Microbiological and geochemical survey of CO_2-dominated mofette and mineral waters of the Cheb Basin, Czech Republic: Frontiers in Microbiology, v. 8, no. 2446.

Kříbek, B., Knésl, I., Rojík, P., Sýkorová, I., and Martínek, K., 2017, Geochemical history of a Lower Miocene lake, the Cypris Formation, Sokolov Basin, Czech Republic: Journal of Paleolimnology, v. 58, p. 169–190.

Krs, M., Krsová, M., Pruner, P., Zeman, A., Novák, F., and Jansa, J., 1990, A petromagnetic study of Miocene rocks bearing micro-organic material and the magnetic mineral greigite (Sokolov and Cheb basins, Czechoslovakia): Physics of the Earth and Planetary Interiors, v. 63, p. 98–112.

Lanson, B., Beaufort, D., Berger, G., Bauer, A., Cassagnabere, A., and Meunier, A., 2002, Authigenic kaolin and illitic minerals during burial diagenesis of sandstones: a review: Clay minerals, v. 37, p. 1–22.

Lau, K.V., and Hardisty, D.S., 2022, Modeling the impacts of diagenesis on carbonate paleoredox proxies: Geochimica et Cosmochimica Acta, v. 337, p. 123–139.

Li, J., Xiao, Y., Feng, X., Wang, J., Ma, Z., Yao, R., Zhai, Y., and Tian, L., 2024, Leaching of ion adsorption rare earths and the role of bioleaching in the process: a review: Journal of Cleaner Production, v. 468, no. 143067.

Liu, Q., Adler, K., Lipus, D., Kämpf, H., Bussert, R., Plessen, B., Schulz, H.M., Krauze, P., Horn, F., Wagner, D., Mangelsdorf, K., and Alawi, M., 2020, Microbial signatures in deep CO_2-saturated Miocene sediments of the active Hartoušov mofette system (NW Czech Republic): Frontiers in Microbiology, v. 11, no. 3182.

Lovley, D.R., and Phillips, E.J.P., 1988, Manganese inhibition of microbial iron reduction in anaerobic sediments: Geomicrobiology Journal, v. 6, p. 145–155.

Lyons, T.W., Tino, C.J., Fournier, G.P., Anderson, R.E., Leavitt, W.D., Konhauser, K.O., and Stüeken, E.E., 2024, Co-evolution of early Earth environments and microbial life: Nature Reviews Microbiology, v. 22, p. 572–586.

Mach, K., Žák, K., Teodoridis, V., and Kvaček, Z., 2017, Consequences of lower Miocene CO_2 degassing on geological and paleoenvironmental settings of the Ahníkov/Merkur Mine paleontological locality (Most Basin, Czech Republic): Neues Jahrbuch für Geologie und Paläontologie-Abhandlungen, v. 285, p. 235–266.

Middelburg, J.J., 2019, Marine carbon biogeochemistry: a primer for earth system scientists: Springer, Briefs in Earth System Sciences, 118 p.

Murad, E., and Rojík, P., 2003, Iron-rich precipitates in a mine drainage environment: influence of pH on mineralogy: American Mineralogist, v. 88, p. 1915–1918.

Murad, E., and Rojík, P., 2005, Iron mineralogy of mine-drainage precipitates as environmental indicators: review of current concepts and a case study from the Sokolov Basin, Czech Republic: Clay Minerals, v. 40, p. 427–440.

Oremland, R.S., and Stolz, J.F., 2003, The ecology of arsenic: Science, v. 300, p. 939–944.

Pačes, T., and Šmejkal, V., 2004, Magmatic and fossil components of thermal and mineral waters in the Eger River continental rift (Bohemian massif, central Europe), *in* Wanty R.B., and Seal, R.R., II, eds., 11th International Symposium on Water–Rock Interactions, Proceedings: Leiden, A.A. Balkema, p. 167–172.

Parkhurst, D.L., and Appelo, C.A.J., 1999, User's guide to PHREEQC (Version 2): a computer program for speciation, batch-reaction, one-dimensional transport, and inverse geochemical calculation: U.S. Geological Survey, Water-Resources Investigations Report 99-4259, 312 p.

Petrash, D.A., Jan, J., Sirová, D., Osafo, N.O.-A., and Borovec, J., 2018, Iron and nitrogen cycling, bacterioplankton community composition and mineral transformations involving phosphorus stabilisation in the ferruginous hypolimnion of a post-mining lake: Environmental Science: Processes and Impacts, v. 20, p. 1414–1426.

Petrash, D.A., Steenbergen, I.M., Valero, A., Meador, T.B., Paces, T., and Thomazo, C., 2022, Aqueous system-level processes and prokaryote assemblages in the ferruginous and sulfate-rich bottom waters of a post-mining lake: Biogeosciences, v. 19, p. 1723–1751.

Posth, N.R., Canfield, D.E., and Kappler, A., 2014, Biogenic Fe(III) minerals: from formation to diagenesis and preservation in the rock record: Earth-Science Reviews, v. 135, p. 103–121.

Poulton, S.W., and Canfield, D.E., 2005, Development of a sequential extraction procedure for iron: implications for iron partitioning in continentally derived particulates: Chemical Geology, v. 214, p. 209–221.

Poulton, S.W., and Raiswell, R., 2002, The low-temperature geochemical cycle of iron: from continental fluxes to marine sediment deposition: American Journal of Science, v. 302, p. 774–805.

Poulton, S.W., Krom, M.D., and Raiswell, R., 2004, A revised scheme for the reactivity of iron (oxyhydr)oxide minerals towards dissolved sulfide: Geochimica et Cosmochimica Acta, v. 68, p. 3703–3715.

Raiswell, R., and Canfield, D.E., 1996, Rates of reaction between silicate iron and dissolved sulfide in Peru margin sediments: Geochimica et Cosmochimica Acta, v. 60, p. 2777–2788.

Raiswell, R., and Canfield, D.E., 2012, The Iron Biogeochemical Cycle Past and Present: Geochemical Perspectives, v. 1, 220 p.

Raiswell, R., Hardisty, D.S., Lyons, T.W., Canfield, D.E., Owens, J.D., Planavsky, N.J., Poulton, S.W., and Reinhard, C.T., 2018, The iron paleoredox proxies: a guide to the pitfalls, problems and proper practice: American Journal of Science, v. 318, p. 491–526.

Rapprich, V., Čáp, P., Erban Kochergina, Y.V., Kadlecová, E., Benkó, Z., Sakala, J., Rodovská, Z., Matějů, J., and Petrash, D.A., 2023, Interactions between distal epiclastic and bio-chemogenic sedimentation at the foothills of a mafic alkaline volcano: the case of the Oligocene Doupovské Hory Volcanic Complex (Czech Republic): The Depositional Record, v. 9, p. 871–894.

Ravel, B., and Newville, M., 2005, Athena, Artemis, Hephaestus: data analysis for X-ray absorption spectroscopy using IFEFFIT: Journal of Synchrotron Radiation, v. 12, p. 537–541.

Reiche, M., Lu, S., Ciobotaŏ, V., Neu, T.R., Nietzsche, S., Rösch, P., Popp, J., and Küsel, K., 2011, Pelagic boundary conditions affect the biological formation of iron-rich particles (iron snow) and their microbial communities: Limnology and Oceanography, v. 56, p. 1386–1398.

Rice, C.A., Tuttle, M.L., and Reynolds, R.L., 1993, The analysis of forms of sulfur in ancient sediments and sedimentary rocks: comments and cautions: Chemical Geology, v. 107, p. 83–95.

Rojík, P., 2004, New stratigraphic subdivision of the Tertiary in the Sokolov Basin in Northwestern Bohemia: Czech Geological Society, Journal, v. 49, p. 173–185.

Rosenbaum, J., and Sheppard, S.M.F., 1986, An isotopic study of siderites, dolomites and ankerites at high-temperatures: Geochimica et Cosmochimica Acta, v. 50, p. 1147–1150.

Saunders, J.K., Fuchsman, C.A., McKay, C., and Rocap, G., 2019, Complete arsenic-based respiratory cycle in the marine microbial communities of pelagic oxygen-deficient zones: National Academy of Sciences [USA], Proceedings, v. 116, p. 9925–9930.

Schulz, K., Notini, L., Grigg, A.R.C., Kubeneck, L.J., Wisawapipat, W., ThomasArrigo, L.K., and Kretzschmar, R., 2023, Contact with soil impacts ferrihydrite and lepidocrocite transformations during redox cycling in a paddy soil: Environmental Science Processes & Impacts, v. 25, p. 1945–1961.

Šmejkal, V., 1978, Oxygen isotopic composition of sulphates from some mineral waters and mine waters in western Bohemia, in Isotope Hydrology 1978: International Atomic Energy Agency Symposium, Neuherberg, Germany 19–23 June, p. 83–97.

Soetaert, K., Hofmann, A.F., Middelburg, J.J., Meysman, F.J.R., and Greenwood, J., 2007, The effect of biogeochemical processes on pH: Marine Chemistry, v. 105, p. 30–51.

Stucki, J.W., 2011, A review of the effects of iron redox cycles on smectite properties: Comptes Rendus Geoscience, v. 343, p. 199–209.

Stucki, J.W., and Kostka, J.E., 2006, Microbial reduction of iron in smectite: Comptes Rendus Geoscience, v. 338, p. 468–475.

Thomazo, C., Brayard, A., Elmeknassi, S., Vennin, E., Olivier, N., Caravaca, G., Escarguel, G., Fara, E., Bylund, K.G., Jenks, J.F., Stephen, D.A., Killingsworth, B., Sansjofre, P., and Cartigny, P., 2019, Multiple sulfur isotope signals associated with the late Smithian event and the Smithian/Spathian boundary: Earth-Science Reviews, v. 195, p. 96–113.

Tostevin, R., 2021, Cerium anomalies and paleoredox, *in* Lyons, T.W., Turchyn, A., and Reinhard, C., eds., Elements in Geochemical Tracers in Earth System Science: Cambridge University Press, v. 7027, 21 p.

Tribovillard, N., 2020, Arsenic in marine sediments: How robust a redox proxy?: Palaeogeography, Palaeoclimatology, Palaeoecology, v. 550, no. 109745.

Turchyn, A.V., and Schrag, D.P., 2006, Cenozoic evolution of the sulfur cycle: insight from oxygen isotopes in marine sulfate: Earth and Planetary Science Letters, v. 241, p. 763–779.

Umbría-Salinas, K., Valero, A., Jan, J., Borovec, J., Chrastný, V., and Petrash, D.A., 2021, Redox-driven geochemical partitioning of metal(loid)s in the iron-rich anoxic sediments of a recently flooded lignite mine pit: Lake Medard, NW Czechia: Journal of Hazardous Materials Advances, v. 3, no. 100009.

Valdés, J.J., Petrash, D.A., and Konhauser, K.O., 2024, A novel in-silico model explores LanM homologs among *Hyphomicrobium* spp.: Communications Biology, v. 7, no. 1539.

Valero, A., Jan, J., and Petrash, D.A., 2023, Anaerobic dissolved As(III) removal from metal-polluted waters by cathode-stabilized Fe(III)-oxyhydroxides: Environmental Science: Water Research and Technology, v. 9, p. 454–466.

Valero, A., Petrash, D.A., Kuchenbuch, A., and Korth, B., 2024, Enriching electroactive microorganisms from ferruginous lake waters: mind the sulfate reducers!: Bioelectrochemistry, v. 157, no. 108661.

Vrzal, D., Přikryl, I., Truszyk, A., and Fafílková, V., 2011, Complicated water quality and stratification at the post-mining pit lake Medard near Sokolov, Czech Republic, *in* Rüde, T.R., Freund, A., and Wolkersdorfe, C., eds., Proceedings of the 11th International Mine Water Association Congress, Mine Water, Managing the Challenges, Aachen, Germany, p. 551–556.

Wang, W., Ding, B., Hu, Y., Zhang, H., He, Y., She, Y., and Li, Z., 2022, Evidence for the occurrence of Feammox coupled with nitrate-dependent Fe(II) oxidation in natural enrichment cultures: Chemosphere v. 303, no. 134903.

Weinlich, F.H., Bräuer, K., Kämpf, H., Strauch, G., Tesař, J., and Weise, S.M., 1999, An active subcontinental mantle volatile system in the western Eger rift, Central Europe: gas flux, isotopic (He, C, and N) and compositional fingerprints: Geochimica et Cosmochimica Acta, v. 63, p. 3653–3671.

Wirth, S.B., Gilli, A., Niemann, H., Dahl, T.W., Ravasi, D., Sax, N., Hamann, Y., Peduzzi, R., Peduzzi, S., Tonolla, M., Lehmann, M.F., and Anselmetti, F.S., 2013, Combining sedimentological, trace metal (Mn, Mo) and molecular evidence for reconstructing past water-column redox conditions: the example of meromictic Lake Cadagno (Swiss Alps): Geochimica et Cosmochimica Acta, v. 120, p. 220–238.

Zhang, K., and Shields, G.A., 2022, Sedimentary Ce anomalies: secular change and implications for paleoenvironmental evolution: Earth-Science Reviews, v. 229, no. 104015.

Received 27 November 2024; accepted 17 April 2025.